



Magnetic coupling and amplitude truncation based bistable energy harvester

Li Zhao ^a, Guobiao Hu ^b, Shengxi Zhou ^c, Yan Peng ^{d,e}, Shaorong Xie ^f, Zhongjie Li ^{a,d,*}

^a School of Mechatronic Engineering and Automation, Shanghai University, Shanghai 200444, PR China

^b Internet of Things Thrust, The Hong Kong University of Science and Technology (Guangzhou), Nansha, Guangzhou, Guangdong 511400, PR China

^c School of Aeronautics, Northwestern Polytechnical University, Xi'an 710072, PR China

^d Institute of Artificial Intelligence, School of Future Technology, Shanghai University, Shanghai 200444, PR China

^e Shanghai Artificial Intelligence Laboratory, Shanghai 200232, PR China

^f School of Computer Engineering and Science, Shanghai University, Shanghai 200444, PR China



ARTICLE INFO

Keywords:

Piezoelectric energy harvester
Double beams
Magnetic coupling
Amplitude truncation
Wide frequency bandwidth
Wide impedance matching range

ABSTRACT

We present a two-degree-of-freedom bistable piezoelectric energy harvester (PEH) combining both magnetic coupling and amplitude truncation mechanisms to improve the electrical response when installed within compact spaces. The PEH processes a time-varying potential well and each beam has two electrical responses due to the interaction between two magnets. The collision-induced amplitude truncation behavior leads to high-frequency vibration responses, which reduces the matching impedance of the PEH. The Hamilton's principle and the Galerkin method was applied to establish the distributed parameter model for the system. By numerical calculations, the influence of the magnet distance and beam stiffness ratio on the static potential well, as well as the influence of excitation acceleration and stop gap on the voltage and power response were explored. A series of experiments were conducted to validate the voltage and power responses under sweep and fixed frequency excitations. The experimental and simulation results agree with each other. Due to the effect of magnetic coupling, the response frequency bandwidth of the cantilever beam widens by more than 7 Hz. The frequency-up effect generated by collision increases the response power of the system with the maximum of 307.8 mW at $10^{3.6}$ Ω in experiments, and the combination of the two widens the impedance matching range of the system. This broadband structure with a wide impedance matching range and limited motion is more suitable for practical applications.

1. Introduction

Energy harvesting technology offers a promising solution to address the global energy crisis. Energy harvesters can supply power to remote wireless sensors for monitoring and analyzing environmental conditions by harnessing energy from the ambient [1–5]. To effectively obtain mechanical energy from the environment, various energy harvesting technologies have emerged in recent years, such as piezoelectric energy harvesters [6–9], frictional energy harvesters [10–12], electromagnetic energy harvesters [13–16], etc. Among diverse energy harvesting methods, piezoelectric energy harvesters (PEHs) have gained substantial attention due to their consistent output performance, lack of electromagnetic interference, relatively simple design, and high adaptability to various scenes [17–19]. However, a notable limitation of a linear PEH is

its narrow operational frequency bandwidth centered around the resonant frequency and narrow workspaces [20–22]. This poses a challenge when attempting to match the broader spectrum of random vibrations present in the ambient environment [23–25]. Therefore, many researchers have proposed innovative approaches to broaden the effective bandwidths and enhance power outputs. These strategies include the implementation of multi-stability technology [26,27], the utilization of amplitude truncation techniques [28,29], and the incorporation of the force/displacement amplifier [30–32] or multi-degree-of-freedom structures [33–35] etc.

Owing to the wider bandwidths compared to their conventional counterparts, multi-stable PEHs have garnered substantial attention from researchers in recent years. The large amplitude inter-well vibrations have been proven beneficial for improving energy harvesting

* Corresponding author at: School of Mechatronic Engineering and Automation, Shanghai University, Shanghai 200444, PR China.

E-mail address: lizhongjie@shu.edu.cn (Z. Li).

performance [36,37]. Atmeh et al. utilized the magnetic coupling effect in piezoelectric harvesters to enhance the power at low frequency by converting the low-frequency vibration to high-frequency vibrations [38,39]. Liu et al. [40] introduced the displacement amplification mechanism into the bistable energy harvester and optimized the prototype with several times higher output performance compared to the unoptimized prototype. Jiang et al. [41] applied a beam-spring and magnets to construct a two-degree-of-freedom (2DOF) bistable energy harvester, whose working bandwidth is improved by more than 60 %. Li et al. [42] investigated the practical asymmetry effect on BEH performance, whose power is improve by 57.56 % in simulation. Zhang et al. [43] proposed a bistable electromagnetic vibration energy harvester based on the internal resonance, whose the bandwidth and the peak power output are increased by 84.3 % and 30.0 % compared with the mistuned model, respectively. Norenberg et al. [44] comprehensively studied the influence of the asymmetric characteristics on the performance of the bistable energy harvester. Liu et al. [45] cleverly added a swinging mass-bar at the free end of a piezoelectric cantilever beam elastically to form a bistable structure. However, a limitation was identified: the deep barrier between potential wells might hinder the snap-through motion under small excitations. To address this challenge, other studies further explored PEHs in tri-stable [46–48], quad-stable [49,50], and penta-stable [51,52] configurations to decrease potential barriers. Costa et al. [53] proposed a compactness and space-efficient energy harvester with unprecedented multistable characteristics. However, it is also important to note that incorporating additional magnets escalates structural complexity and intricacies.

Another technique to utilize spatial limitations and enlarge the operational bandwidth is the amplitude truncation technique (ATT) [54–57]. Zhou et al. [58] compared the dynamic characteristics and output performance of various PEHs, considering different collision stiffness, locations and initial gap sizes. Machado et al. [59] proposed an innovative rotational PEH with a spring stop mechanism. It could generate a rectified power ranging from 102 μW to 845 μW across rotational speeds from 50 to 150 rpm. Xiao et al. [60] utilized friction and impact to achieve self-exciting vibration, which explored the potential of frictional signals in monitoring applications. Tan et al. [61] combined the sliding mode and impact mode of the triboelectric nanogenerators (TENGs) working principle to enhance the efficiency of harvesting energy from low-frequency vibration. Fang et al. [62] utilized the centrifugal softening and impact to improve the power density in ultra-low-frequency rotational energy harvesting. Bahmanziari et al. [63] combined magnetic plucking, mechanical impact, and mechanical vibration force to obtain average power of 13.6 mW from piezoelectric smart tiles. Xu et al. [64] applied the stoppers to achieve a maximum ratio of triple and essential frequency components reaching up to 8.86. Sokolov et al. [65] applied the impact from stoppers to produce the frequency up-conversion effect in a microscopic electrostatic harvester. Alvis et al. [66] investigated that a soft stopper and a stop gap of 5 mm performs the most effectively in energy harvesting from vortex-induced vibrations. He et al. [67] exposed that the peak voltage of the 2DOF PEH with an elastic stopper is 12.82 times and 3.47 times the output voltage of the NPEH without the stopper at the first and second resonance. Hassan et al. [68] utilized multi-modality and piecewise linearity to construct a 2DOF vibro-impact TENG, which increases output voltage by more than 300 %, and the bandwidth by 250 %. The ATT technique serves a dual purpose: widening the bandwidth and reducing the required working space for PEHs. This feature renders certain PEHs suitable for working in limited spaces, such as vehicle suspensions, wheel hubs and engine compartments, where inevitable collisions occur between the PEH and mechanical structures. In this way, the ATT technique improves both the performance and practical applicability of energy harvesters.

In addition to the aforementioned technologies, designing multi-degree-of-freedom (MDOF) PEHs for multi-modal energy harvesting has also garnered significant attention. Shao et al. [69] introduced a

two-degree-of-freedom (2DOF) PEH design that could effectively operate within a bandwidth of 11.0 Hz. Zhang et al. [70] employed three piecewise-linear PEHs to expand the operating frequency bandwidth by 90.0 % under an acceleration of 10 m/s^2 . Through meticulous comparative studies, Li et al. [71] demonstrated that a 2DOF bistable energy harvester produced a substantially larger power output than a linear counterpart. Wang et al. [72] proposed a 2DOF bistable PEH with an additional parasitic oscillator attached to the primary structure. This setup yielded two resonant peaks with robust nonlinear Dynamic. Kim et al. [73] proposed a MDOF vibration system as the TENG structure with several resonant frequencies. Zhang et al. [74] mounted 2DOF nonlinear bistable absorbers periodically to achieve broadband multi-frequency vibration. Hao et al. [75] designed a three-degree-of-freedom TNG with the power of 27.01 mW under the movement speed of 8 km/h per person. MA et al. [76] produced a dual-beam piezo-magneto-elastic energy harvester reaching 4.9×10^{-4} W at the wind speed of 10.2 m/s. He et al. [77] introduced an auxetic structure to a MDOF PEH, which improves the output power in the first mode up to 2548 % compared to a conventional PEH. Ding et al. [78] introduced fractal topology into a PEH, whose the efficient energy harvesting bandwidth under iterative levels 1 and 2 is 2.05 and 2.15 times larger than the conventional PEHs, respectively. Fan et al. [79] designed a PEH with a middle beam and two side beams, which possesses multiple resonance regions and an wider effective frequency bandwidth. Liu et al. [80] proposed a 2DOF marine energy harvester to capture energy of currents and winds from ocean with a maximum power of 44.18 W. MDOF PEHs have demonstrated their ability to greatly improve energy harvesting performance in various operational conditions and scenarios [81–83].

Some researchers have combined magnetic coupling technology with MDOF technology, which enhanced the output performance of PEHs. Atmeh et al. utilized magnetic coupling to couple cantilever beams with different lengths to achieve up conversion, achieving the conversion of low-frequency vibration to high-frequency [38]. Cong et al. [84] utilized a magnetically coupled cantilever beam array, Shao et al. [85] placed the two beams orthogonally through magnetic coupling, Noh et al. studied out-of-phase and in-phase mode regimes magnetic coupling cantilever beams [86], and Li et al. proposed a U-shaped magnetic 2DOF PEH [87] to obtain a broadband high-power output. Although these contributions have improved the efficiency of energy harvesters through magnetic coupling, they have not taken into account the impact of space constraints on the output performance of energy harvesters. Based on these previous studies, we proposed a two-degree-of-freedom bistable piezoelectric energy harvester coupling two beams through the magnetic interaction restricted within a compact space with limited vibration.

The primary contributions of this study are as follows. Firstly, the distributed parameter model was established based on the extended Hamilton's principle and the Galerkin method. Secondly, the effects of key parameters on potential wells, voltage, and power performance were discussed. Third, a series of experiments were conducted to verify the numerical calculation results. The introduction of this novel harvester concept, exploration of critical parameters, comprehensive power analysis, and experimental validation collectively advance the understanding and practical applications of such energy harvesting systems. This paper is organized as follows: The configuration is designed and the mathematical model is established in Section 2. The key parameters affecting the elastic potential energy and frequency-voltage response are discussed in Section 3. Section 4 exhibits the influence of magnet distance, stop gap, excitation frequency, and external resistance on the power and voltage output. In Section 5, a prototype is fabricated and a series of experiments are conducted to validate the numerical results. Section 6 draws conclusions.

2. System design and modeling

In ambient environments and mechanical systems, energy harvesting devices often face the challenges of an insufficient operational space and narrowband issues [21,53]. This limitation restricts their range of motion, leading to deteriorated energy harvesting performance. To address this practical concern, we introduce the design of an impact-based magnetically-coupled two-degree-of-freedom piezoelectric energy harvester (IMTPEH). Unlike conventional bistable PEHs, which do not consider motion limitations and variable potential wells, this novel design is well-suited for scenarios with restricted space, such as engine compartments. As illustrated in Fig. 1(a), the proposed IMTPEH configuration incorporates two inverted cantilever beams rigidly affixed to a base. The free ends of these cantilevers are equipped with magnets facing each other with identical poles. Two piezoelectric patches are bonded onto the upper surfaces of the metallic cantilevers. The oscillation amplitudes of the magnets are constrained by two stoppers mounted on the base. The number and positions of the stoppers may vary and affect the amplitude restriction on the magnets. These aspects will be explored and discussed in the following of this paper.

The geometric arrangement of the IMTPEH is depicted in Fig. 1(b). The inertial coordinate system is denoted as \mathbf{e}_x and \mathbf{e}_y . \dot{w}_b , as the external excitation, is assumed to be in the sinusoidal form $\text{Asin}(2\pi ft)$, characterized by an acceleration amplitude A and an excitation frequency f .

Although the size and mechanical properties of piezoelectric patches are relatively small compared to the base beam, they slightly increase the natural frequency of the system. Therefore, as of modeling, the beam is divided into two parts: a composite beam with attached piezoelectric patch and a base beam without attached piezoelectric patch. The electromechanical coupling dynamic model of the IMTPEH can be formulated using the energy method grounded in Hamilton's principle [58, 59]. The kinetic energy of the IMTPEH can be expressed as follows:

$$T_k = \sum_{i=1}^2 \frac{1}{2} \left\{ \rho_{Ci} A_{Ci} \int_0^{L_{Pi}} [\dot{w}_i(x, t) + \dot{w}_b(t)]^2 dx + \rho_{Bi} A_{Bi} \int_{L_{Pi}}^{L_{Bi}} [\dot{w}_i(x, t) + \dot{w}_b(t)]^2 dx + m_{Mi} [\dot{w}_i(L_{Bi}, t) + \dot{w}_b(t) + b_i \dot{w}'_i(L_{Bi}, t)]^2 + I_i \dot{w}'_i^2(L_{Bi}, t) \right\}, \quad (1)$$

where ρ_{Ci} and L_{Ci} are the material density and the length of the i th composite beam, respectively, where $i = 1, 2$. Here, 1 and 2 correspond to A and B, respectively, which will not change unless stated separately. ρ_{Bi} and L_{Bi} are the material density and the length of i th base beam, respectively. m_{Mi} and I_i are the mass and the inertia of the i th magnet, respectively. $w_i(x, t)$ is the deflection of the i th beam; b_i is the distance from the centroid of the i th magnet to the fixed point on the cantilever beam. $A_{Ci} = b_{Ci} \cdot h_{Ci}$ and $A_{Bi} = b_{Bi} \cdot h_{Bi}$ are the cross-sectional area of the i th composite beam and base beam, respectively, where b_{Cb} , b_{Bb} , h_{Cb} , h_{Bi} are the corresponding widths and thicknesses, respectively.

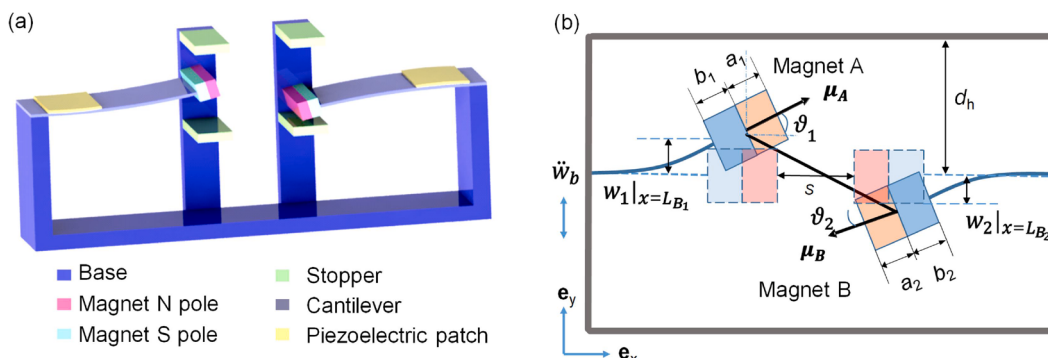


Fig. 1. Proposed piezoelectric energy harvester: (a) Schematics diagram. It consists of two beams coupled by two magnets fixed at the end of the free ends and four stoppers to the limit motion (b) geometric configuration. w_i represents the lateral displacement of Beam i , where $i=1, 2$ represents A and B, respectively.

The elastic potential energy stored in the two inverted beams and the piezoelectric patches mounted on them can be expressed as follows:

$$U_C = \sum_{i=1}^2 \frac{1}{2} \left(E_{Ci} I_{Ci} \int_0^{L_{Pi}} w_i''^2(x, t) dx + E_{Bi} I_{Bi} \int_{L_{Pi}}^{L_{Bi}} w_i''^2(x, t) dx - e_{31} H_{Pi} \frac{V_{Pi}(t)}{h_{Pi}} \int_0^{L_{Pi}} w_i''(x, t) dx \right), \quad (2)$$

where e_{31} , H_{Pi} and $V_{Pi}(t)$ are the effective piezoelectric stress constant, and output voltage of the i th piezoelectric patch, respectively. $E_{Ci} I_{Ci}$ and $E_{Bi} I_{Bi}$ are the bending stiffness of the i th composite beam and base beam, respectively, whose specific forms are given in 'Appendix A'.

The electric energy of the system is the work done by the electric field intensity in the piezoelectric layer on the potential shift [38,39] given by:

$$W_E = \frac{1}{2} \sum_{i=1}^2 \left[\varepsilon_{33}^{P_i} L_{Pi} b_{Pi} V_{Pi}^2(t) + \frac{e_{31}}{h_{Pi}} V_{Pi}(t) H_{Pi} \int_0^{L_{Pi}} w_i''(x, t) dx \right], \quad (3)$$

where $\varepsilon_{33}^{P_i}$ is the piezoelectric material permittivity constant of the i th piezoelectric patch, respectively. The point dipoles model is used to describe the magnets in the energy harvester following Ref. [25].

The distance \mathbf{r}_{AB} from the source of Magnet A to Magnet B is given by:

$$\mathbf{r}_{AB} = [s + a_1 + a_2 + a_1(1 - \cos\theta_1) + a_2(1 - \cos\theta_2)] \mathbf{e}_x + [w_1|_{x=L_{B1}} + b_1 \sin\theta_1 - w_2|_{x=L_{B2}} - b_2 \sin\theta_2] \mathbf{e}_y, \quad (4)$$

while the reverse distance \mathbf{r}_{BA} is given by:

$$\mathbf{r}_{BA} = [s + a_1 + a_2 + a_1(1 - \cos\theta_1) + a_2(1 - \cos\theta_2)] \mathbf{e}_x - [w_1|_{x=L_{B1}} + b_1 \sin\theta_1 - w_2|_{x=L_{B2}} - b_2 \sin\theta_2] \mathbf{e}_y, \quad (5)$$

where s and a_i are the distance between the opposite faces of two magnets, and the distances from the centroid to the front face of the i th magnet, respectively. $w_i|_{x=L_{Bi}}$ is the tip lateral displacement with a small rotation angle $\theta_i = \theta'_i(L_{Bi}, t)$ of the i th base beam.

The two magnetic dipole moment vectors are given by:

$$\boldsymbol{\mu}_A = M_{M1} V_{M1} \cos\theta_1 \mathbf{e}_x + M_{M1} V_{M1} \sin\theta_1 \mathbf{e}_y, \quad (6)$$

$$\boldsymbol{\mu}_B = -M_{M2} V_{M2} \cos\theta_2 \mathbf{e}_x - M_{M2} V_{M2} \sin\theta_2 \mathbf{e}_y, \quad (7)$$

where M_{M1} and V_{M1} are the magnetization intensity and the volume of the i th magnet, respectively.

The magnetic fields produced by Magnet A and Magnet B interacting with each other are given by:

$$B_{AB} = -\frac{\mu_0}{4\pi} \nabla \frac{\boldsymbol{\mu}_A \mathbf{r}_{AB}}{\|\mathbf{r}_{AB}\|_2^3}, \quad (8)$$

$$B_{BA} = -\frac{\mu_0}{4\pi} \nabla \frac{\boldsymbol{\mu}_B \mathbf{r}_{BA}}{\|\mathbf{r}_{BA}\|_2^3}, \quad (9)$$

where ∇ and $\|\cdot\|_2$ denote vector gradient operator and Euclidean norm, respectively.

The magnetic potential energy of the system can be represented as follows:

$$U_M = -B_{AB} \cdot \boldsymbol{\mu}_B - B_{BA} \cdot \boldsymbol{\mu}_A, \quad (10)$$

where the specific expression of U_M is given in 'Appendix A'. Due to the limitation of stoppers on the lateral displacement of the cantilever beams, the rotation angle ϑ_i of the end magnet is small. Therefore, we can take the following approximations: $\sin \vartheta_i \rightarrow 0$, $\cos \vartheta_i \rightarrow 1$, $i = 1, 2$. The magnetic forces of Magnet A and Magnet B interacting with each other along the \mathbf{e}_y axis can be derived according to $F_{Mi} = \nabla U_M$ and the above approximations, whose specific forms are given in 'Appendix A'. A piecewise linear function [44,45] is used to describe the nonlinear impact force as follows:

$$F_{S_i}(L_{S_i}, t) = \begin{cases} k_{si}[w_i(L_{B_i}, t) + dw'_i(L_{B_i}, t) - d_{hi}] & w_i(L_{B_i}, t) + dw'_i(L_{B_i}, t) > d_{hi} \\ 0 & -d_{hi} < w_i(L_{B_i}, t) + dw'_i(L_{B_i}, t) < d_{hi} \\ k_{si}[w_i(L_{B_i}, t) + dw'_i(L_{B_i}, t) + d_{hi}] & w_i(L_{B_i}, t) + dw'_i(L_{B_i}, t) < -d_{hi} \end{cases} \quad (11)$$

where k_{si} and d_{hi} represent the impact stiffness and the gap between the stopper and the i th magnet, respectively. Once the magnet displacement exceeds the range of $\pm d_h$, the magnet collides with the stop block. This collision reinforces the structural rigidity of the cantilever beam, leading to a pronounced high-frequency response. The magnet does not collide if the cantilever beam undergoes motion within the interval of $(-d_h, d_h)$.

The work done by external force mainly includes three parts: the work done by the electric charge when passing through the resistance, the work done by the internal resistance of the cantilever beam, and the work generated by the collision. Therefore, the work done by external force can be expressed as follows:

$$\delta W_C = -Q_i(t)\delta V_i(t) - \int_0^{L_{B_i}} F_{S_i}(L_{B_i}, t)\delta(x - L_{B_i})\delta w_i dx - \int_{V_i} c_i \frac{\partial S_i}{\partial t} \delta S_i dV_i, \quad (12)$$

where δ is the variational operator, c_i and S_i are the damping coefficient and transverse strain of the i th beam, respectively. The Galerkin discretization [59] is employed to separate the displacement response of the cantilever beam into spatial and time components as:

$$w_i(x, t) = \sum_{j=1}^{\infty} \eta_{ij}(t) \phi_{ij}(x), \quad (13)$$

where $\eta_{ij}(t)$ is the generalized temporal coordinates and $\phi_{ij}(x)$ is the model shape function with two segments changed due to the geometric and material characteristics.

$$\phi_{ij}(x) = \sum_{n=1}^2 \phi_{ijn}(x) H_{in}(x), \quad (14)$$

where $H_{ijn}(x)$ is the Heaviside step function with 1 or 0 according to the boundary condition. $\phi_{ij1}(x)$ is the shape function of the composite beam, while $\phi_{ij2}(x)$ represents the base beam. Their detailed expressions are given in "Appendix A".

To effectively depict the high-frequency vibrational response resulting from collisions, this paper adopts the first three orders of beam modes to characterize the behavior of the cantilever beam. The Lagrange function of the system can be written as follows:

$$L_K = T_K + W_E - U_C - U_M. \quad (15)$$

We take η_{ij} and V_{Pi} as the generalized coordinates and take partial derivatives of the Lagrange equation:

$$\frac{d}{dt} \left(\frac{\partial L_K}{\partial \dot{\eta}_{ij}} \right) - \frac{\partial L_K}{\partial \eta_{ij}} = \frac{\delta W_C}{\delta \eta_{ij}}, \quad (16)$$

$$\frac{d}{dt} \left(\frac{\partial L_K}{\partial \dot{V}_{Pi}} \right) - \frac{\partial L_K}{\partial V_{Pi}} = \frac{\delta W_C}{\delta V_{Pi}}. \quad (17)$$

The electromechanical coupling equation of the IMTPEH can be obtained as follows:

$$\begin{aligned} M_{eij}\ddot{\eta}_{ij}(t) + C_{eij}\dot{\eta}_{ij}(t) + K_{eij}\eta_{ij}(t) - F_{Mi}(t) - \theta_{Pij}V_{Pi}(t) \\ = -\phi_{ij2}(L_{B_i})F_{S_i}(L_{S_i}, t) - \Gamma_{ij}\ddot{w}_b(t), \end{aligned} \quad (18)$$

$$C_{P_i}\dot{V}_{Pi}(t) + \frac{1}{R_{L_i}}V_{Pi}(t) + \sum_{j=1}^3 \theta_{Pij}\dot{\eta}_{ij}(t) = 0, \quad (19)$$

where M_{eij} , C_{eij} , K_{eij} , θ_{Pi} and Γ_{ij} are the electromechanical coupling and excitation coefficients of the i th beams in the j th mode, respectively. R_{L_i} is the load resistance of the i th piezoelectric patch. The specific expressions of M_{eij} , C_{eij} , K_{eij} , θ_{Pi} , and Γ_{ij} can be found in "Appendix A". From Eq. (18), the interaction between Beam A and Beam B is influenced by the magnetic force $F_{Mi}(t)$, and the magnetic force is also affected by the relative position of the two beams. When the resonance frequencies of two beams are different, under the action of the magnets, each beam will move under the excitation of the two resonance frequencies, resulting in two voltage segments.

3. System dynamics analysis

To gain deeper insights into the power generation capability of the IMTPEH, it is imperative to investigate the interactive potential energy and the voltage-frequency response of the system across varying magnet distances and beam stiffness.

3.1. The static potential energy

The static potential energy of the system consists of the elastic potential energy of the cantilever beam and the magnetic potential energy between two magnets, expressed as follows:

$$U_S = \sum_{i=1}^2 \frac{1}{2} K_{eil} w_i^2(L_{B_i}) + U_M. \quad (20)$$

Fig. 2 illustrates the effects of the magnet distance and cantilever stiffness on the potential energy of the system. In **Fig. 2(a.1)**, potential energy surfaces enclosed by three types of boundary lines correspond to magnet distances of 20, 25, and 30 mm, respectively. The black planes denote the positions of the stop blocks, situated at 3 mm and 8 mm, respectively. An analysis of the projected contour of the potential energy surface reveals that with an increase in the magnet distance, the static equilibrium point of the cantilever beams gravitates along a diagonal line. Concurrently, as the magnet distance increases, the magnetic potential energy decreases until the nonlinear state of the bistable diminishes. The bistable system transits to a monostable state when the magnet distance exceeds a critical value as shown in Fig. A1, which is 32 mm. The distribution of static equilibrium points along the diagonal line is attributed to the unaltered stiffness ratio of the two cantilever beams. The presence of a stop block exerts constraints on the static equilibrium position of the system. For the stop gap of 8 mm, the static equilibrium position w_1 of Beam A faces constraints, preventing it from reaching the equilibrium position due to the stop block. However, Beam B remains largely unaffected. When the stop gap reduces to 3 mm, both Beam A and B encounter spatial limitations, rendering the attainment of their

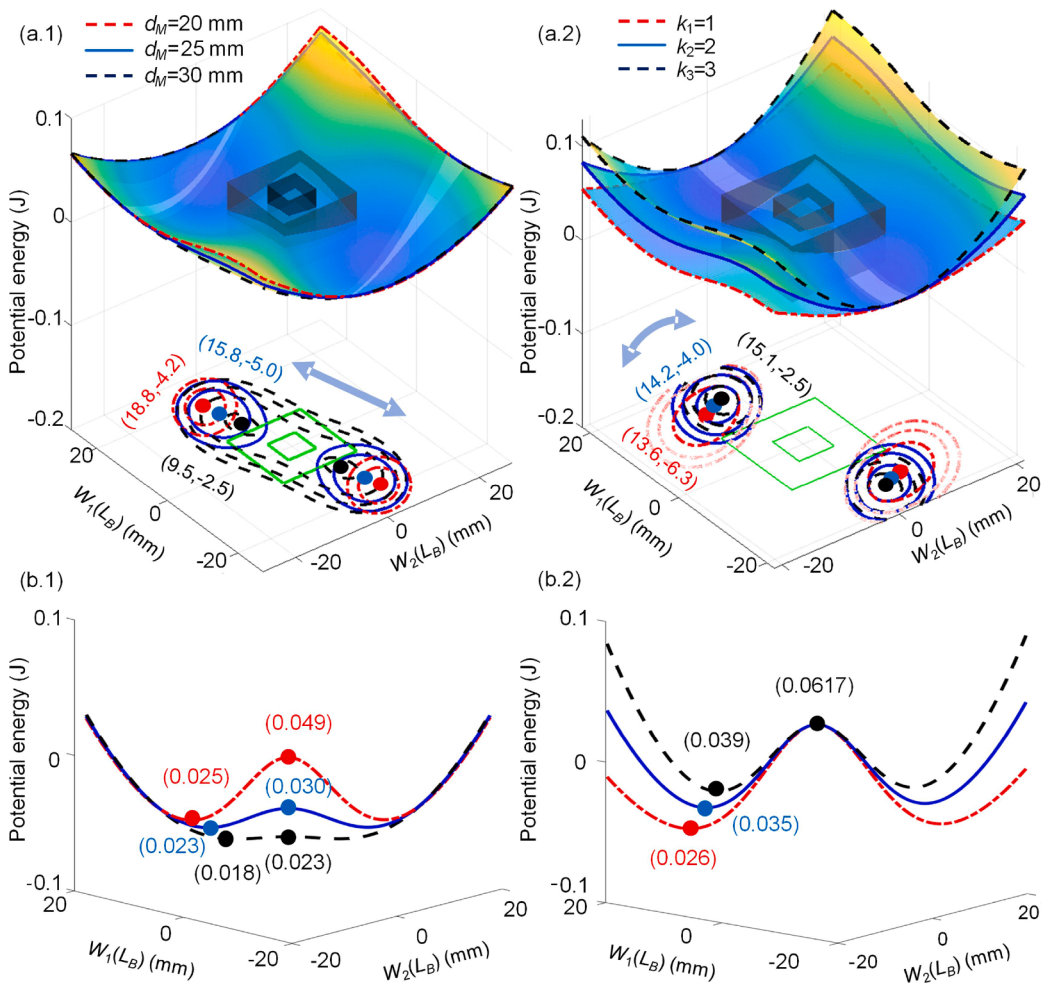


Fig. 2. System potential energy plots under magnet distances of 20, 25 and 30 mm and the stiffness ratio of 1, 2, 3. Three-dimensional potential well surfaces and potential well contours under (a.1) the three magnet distances, (a.2) the stiffness ratio of 1, 2 and 3. Black tetrahedrons represent restricted spaces with stop gaps of 3 and 8 mm, respectively. (b) Curved lines on the potential energy surfaces along the direction $w_1 = w_2$ in Fig. 2(a). The static potential of the system increases with decreasing the magnet distance or increasing the stiffness ratio.

respective equilibrium positions unfeasible. As the restraint distance diminishes, there is a proportional escalation in the energy associated with the orbital movement of the cantilever beam, resulting in an augmented potential energy reservoir within the system. Moving to Fig. 2(b.1), the curved lines on the potential energy surfaces follow the $w_1 = w_2$ direction observed in Fig. 2(a.1). As the magnet distance increases, the height of the potential barrier diminishes, resulting in the gradual approach of the static equilibrium point and a consequent reduction in the overall potential energy. This reduction in potential energy lowers the energy required for the cantilever beam to move across the well.

Fig. 2(a.2) and (b.2) depict the influence of the equivalent stiffness ratio of Beam B to Beam A on the potential well of the system along with varying stopper positions. The projection profile (contour line range: 0.03 - 0.05 J) of the potential well reveals that as the stiffness ratio escalates, the static equilibrium position rotates clockwise. This phenomenon is attributed to the increase in the stiffness of Beam B, leading to a reduction in static deformation. With the augmentation of the stiffness of Beam B, the static equilibrium displacement of Beam B undergoes reduction, eventually contracting to a point within the range of the stop gap. From Fig. 2(b.2), the positions of stop blocks are 8 mm and 3 mm, respectively. As the stiffness ratio increases, Beam B exhibits a reduced susceptibility to the influence of the stopper, while Beam A remains virtually unaffected by the presence of the stopper. When the stop gap is 3 mm, both beams are influenced by the stop blocks in their

static equilibrium positions. Moving to Fig. 2(b.2), with an increase in the stiffness ratio, the overall potential energy of the system rises. At the same time, the potential well gets shallower and narrower. Consequently, the cantilever beams demand more energy to traverse across the well, resulting in a high risk of confined intra-well motion with reduced amplitude under the same acceleration excitation. Since the magnet distance remains constant, the static potential saddle of the system remains unaltered. In other words, the energy required for inter-well movement of the two beams remains consistent. As the stiffness of Beam B increases, the static equilibrium point of the system rotates clockwise. This indicates a decrease in static deformation of Beam B and a subsequent elevation in the overall potential energy, as graphically presented in Fig. 2(b.2). Furthermore, this alteration leads to an increase in stable lateral displacement of Beam A while the displacement of Beam B diminishes. Consequently, Beam A experiences larger amplitudes during inter-well motions than Beam B.

In summary, as the distance of the magnet decreases, the potential barrier elevates, impeding the inter-well motion of the cantilever beam. In contrast, an increase in the stiffness of the cantilever beam elevates the overall potential energy and reduces the relative potential barrier. The stop block restricts the static equilibrium position of the cantilever beam. As the stop gap reduces, the orbital energy of the motion intensifies, thereby heightening the challenge of the inter-well motion of the cantilever beam.

3.2. The frequency voltage response

Following the potential energy analysis, it becomes evident that the magnet distance, stop gap and beam stiffness significantly influence the dynamic motion of an IMTPEH, and further affect the electric output. As a result, this section delves into how the external excitation, magnet distance, stop gap, and beam stiffness collectively influence the open circuit voltage of the system. To comprehensively understand how these factors effect energy harvesting performance, numerical simulations are conducted to obtain the frequency-voltage responses under varying conditions. To better simulate the high-frequency signals generated by collisions, and for ease of calculation, we selected the first three modes. We have verified the rationality of the third-order mode through the comparison results in Fig. A3. Notably, the primary parameters of the IMTPEH are listed in Table 1. The Runge-Kutta method in Matlab software is utilized to obtain voltage-frequency-resistance responses by solving Eqs. (18) - (21) in a vector space, as shown in Eq. (A18).

Fig. 3 illustrates the numerically computed terminal voltage at the external resistance of $10\text{ M}\Omega$ by considering variations in these four influencing factors.

Fig. 3(a) presents the terminal voltage variations as the excitation acceleration increases from 0.4 g to 0.8 g while maintaining the magnet distance at 25 mm and the stop gap at 8 mm . To clearly describe the electrical response of the two beams, we define the voltage response induced by resonance as the active voltage (AV) response and the voltage response induced by magnetic force as the driven voltage (DV) response. In this scenario, for Beam A, the AV peak reaches 34.5 V , and the DV peak is 13.6 V . Likewise, Beam B exhibits an AV peak of 56.0 V and a DV peak of 21.2 V . Although elevating the excitation acceleration amplifies the resonant amplitude, the output peak voltages of the PEHs remain relatively constant due to the displacement restriction enforced by the stop block. Moreover, with increasing excitation acceleration, the truncation frequency bandwidth of Beam A expands from 5.7 Hz to 8.4 Hz and that of Beam B from 0.5 Hz to 2.8 Hz . The increased excitation force prompts a larger displacement of beams as indicated by Eq. (11), and intensifies the impact force between the magnets and the stoppers. This impact force can be likened to augmenting the stiffness of the cantilever beam. However, since Beam B has a higher stiffness than Beam A, the stiffness effect of the magnetic force is more pronounced on Beam A than on Beam B. Consequently, as the excitation force escalates, the truncation frequency band of Beam A surpasses that of Beam B.

Table 1
Material characteristics and geometric parameters of the IMTPEH.

	Parameter	Value
Piezoelectric layer	Beam A: Length \times Width \times Thickness ($L_{B1} \times b_{B1} \times h_{B1}$)	$66\text{ mm} \times 20\text{ mm} \times 0.3\text{ mm}$
	Beam B: Length \times Width \times Thickness ($L_{B2} \times b_{B2} \times h_{B2}$)	$66\text{ mm} \times 20\text{ mm} \times 0.4\text{ mm}$
	Density (ρ_B)	7850 kg/m^3
	Young's modulus (E_B)	200 GPa
	damping coefficient (c_1, c_2)	$12 \times 10^{-7}, 7 \times 10^{-7}$
	Length \times Width \times Thickness ($L_P \times b_P \times h_P$)	$20\text{ mm} \times 20\text{ mm} \times 0.2\text{ mm}$
	Density (ρ_P)	7750 kg/m^3
	Young's modulus (E_P)	90 GPa
	Permittivity constant (ϵ_{33}^P)	$102.2 \times 10^{-9}\text{ F/m}$
	Stress constant (ϵ_{31})	16.6 C/m^2
Permanent magnets	Magnet A: Length \times Width \times Thickness ($L_{M1} \times b_{M1} \times h_{M1}$)	$8\text{ mm} \times 20\text{ mm} \times 8\text{ mm}$
	Magnet B: Length \times Width \times Thickness ($L_{M2} \times b_{M2} \times h_{M2}$)	$8\text{ mm} \times 20\text{ mm} \times 8\text{ mm}$
	Magnet A: residual flux density (B_A)	1.5 T
	Magnet B: residual flux density (B_B)	1.5 T
	Permeability of free space (μ_0)	$4 \times \pi \times 10^{-7}$
Stoppers	Density (ρ_M)	7500 kg/m^3
	Length \times Width \times Thickness ($L_S \times b_S \times h_S$)	$25\text{ mm} \times 30\text{ mm} \times 5\text{ mm}$
	Density (ρ_S)	2700 kg/m^3

Fig. 3(b) reveals the effect of the magnet distance on the voltage response, given a stop gap of 8 mm , an acceleration of 0.6 g and two beam thicknesses of 0.3 mm and 0.4 mm . As the magnet distance increases from 25 mm to 40 mm , the truncation frequency bandwidth of Beam A shrinks from 6.7 Hz to 2.9 Hz , while that of Beam B decreases from 1.3 Hz to 0.4 Hz . Simultaneously, reducing the magnet distance prompts the static equilibrium points to separate away, accentuates the hardening effect and leads to heightened amplitudes in the inter-well motion. This, in turn, triggers an increase in both driven vibration and voltage amplitude across the two beams. The calculated values in Fig. A2 show that when the distance between the magnets is less than the critical value, the natural frequencies of the two beams rapidly increase and stabilize at 13.1 Hz and 19.4 Hz , respectively. However, from Fig. 3(b), as the distance between the magnets decreases, the voltage response frequency of the two beams decreases. This is because as the distance between the magnets decreases, the displacement of the static equilibrium point increases. From Fig. 2(a), when the magnet distance is 25 mm , the static equilibrium point of Beam A has exceeded the limit position of the stopper. The dynamic energy is transmitted to Beam A through collision from stoppers allowing Beam A to vibrate earlier. However, once the magnet distance reduces below a certain threshold, the external excitation acceleration provided by the simulation is insufficient to trigger the complete inter-well motion. For instance, when the magnet distance is 20 mm , the system exhibits confined intra-well oscillations, as depicted in Fig. 3(b).

In Fig. 3(c), the voltage-frequency response of the system is obtained under an acceleration of 0.6 g and a magnet distance of 25 mm . As the stop gap widens, several significant trends emerge: for Beam A, the AV peak increases from 17.9 V to 34.2 V , with a DV of 11.7 V . Meanwhile, for Beam B, the AV peak rises from 28.3 V to 58.2 V , accompanied by a DV of 11.4 V . Increasing the stop gap augments the permissible vibration amplitude of the cantilever beam, causing its motion trajectory to extend toward the bottom of the potential well. This shift makes passing through static equilibrium points easier and facilitates the mutual conversion of kinetic and potential energy, ultimately generating higher output voltages. The DV of Beam A is influenced by both motion of Beam B and the gap between the magnets and stoppers. Hence, the voltage output trend of Beam B aligns with that of Beam A. Notably, as the stop gap increases, the active vibration amplitude truncation frequency bandwidth of Beam A exhibits a minor alteration. In contrast, while that of Beam B decreases from 5.7 Hz to 1.2 Hz .

Fig. 3(d) illustrates the effect of cantilever beam stiffness on the voltage response given a stop gap of 8 mm , a magnet distance of 25 mm , and an excitation acceleration of 0.6 g . When the stiffness of both beams are identical, the electrical performance of the two piezoelectric layers on the beams remains consistent due to their similar dynamic characteristics. As the stiffness of Beam B escalates, its resonant frequency and corresponding voltage response increase. Furthermore, the heightened elastic potential energy of Beam B increases the overall potential energy. Consequently, the inter-well motion of Beam B necessitates more external energy input.

In conclusion, external excitation significantly influences the voltage output of the system. A greater excitation force facilitates the inter-well motion of the two beams, and a reduced magnet distance leads to a larger distance between two static equilibrium points. Hence, piezoelectric ceramic patches exhibit enhanced output voltages and wider response bandwidths when subjected to larger excitation forces and shorter magnet distances. However, the presence of stop blocks constrains the system's voltage output and can even force the beams into higher energy orbits, effectively inducing the beam hardening effect. Furthermore, an increase in the stiffness ratio between the cantilever beams leads to an expansion of the response bandwidth.

4. Electrical performance study

The results presented in Section 3 underscore how the magnet

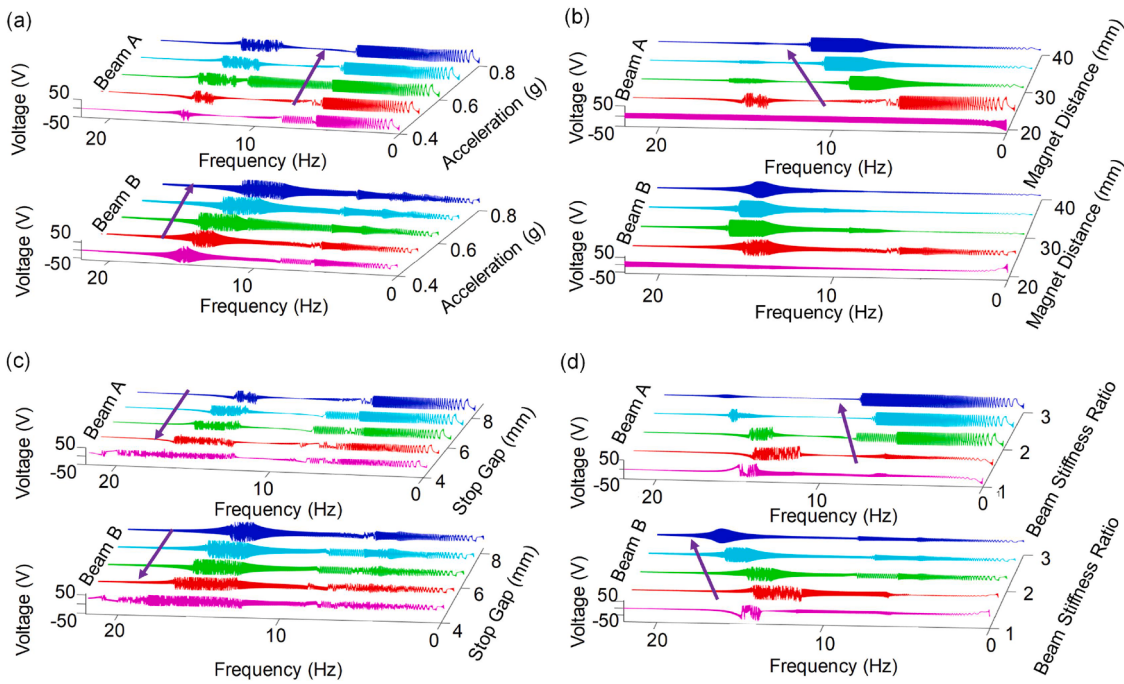


Fig. 3. Numerical results of the voltage response of the IMTPEH under the excitation frequency from 0 Hz to 22.0 Hz. The voltage response bandwidth widens as (a) the excitation acceleration increases from 0.2 g to 0.8 g, (b) the magnet distance increases from 20 mm to 40 mm, (c) the stop gap decreases, and (d) the cantilever beam stiffness ratio increases.

distance and stop gap influence the voltage response of the IMTPEH. To comprehensively understand electrical characteristics of the harvester, Eq. (20) and (21) are employed to calculate the instantaneous power and voltage output under the external resistance R_i generated by the two beams.

$$P_{Ri} = \frac{V_i^2}{R_i}, \quad (21)$$

$$V_{Ri} = |V_i|, \quad (22)$$

where V_i is the instantaneous voltage of the i th patch under the external resistance of R_i , P_{Ri} is the instantaneous power of i th patch, and V_{Ri} is the absolute value of the instantaneous voltage.

Four representative operational scenarios are selected to investigate the power performance, each corresponding to a different installation setup. For the sake of clarity, we designate them as follows: the conventional PEH signifies the energy harvester without magnets and stoppers, α -IMTPEH denotes the harvester with a magnet distance of 30 mm and a stop gap of 8 mm, β -IMTPEH with a magnet distance of 30 mm and a stop gap of 3 mm, γ -IMTPEH with a magnet distance of 25 mm and a stop gap of 8 mm, and δ -IMTPEH with a magnet distance of 25 mm and

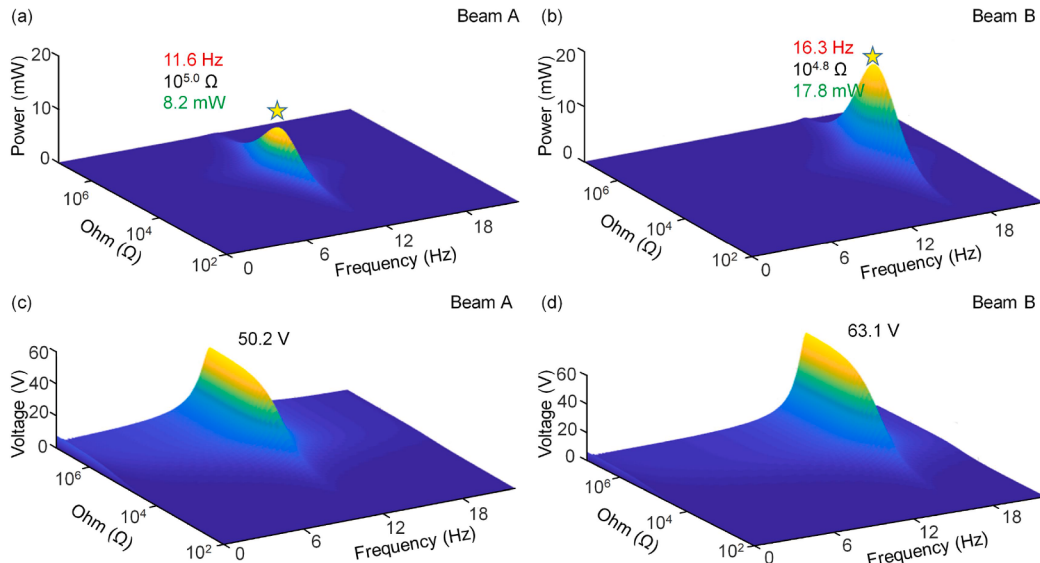


Fig. 4. Numerical results of the power-frequency-resistance responses of (a) Beam A and (b) Beam B and voltage-frequency-resistance responses of (c) Beam A and (d) Beam B in the conventional PEH under the frequency sweep excitation ranging from 0 Hz to 22.0 Hz and the external resistance ranging from $10^{2.0} \Omega$ to $10^{7.0} \Omega$. The maximum power of Beam A is 8.2 mW at 11.6 Hz and $10^{5.0} \Omega$, while that of Beam B is 17.8 mW at 16.3 Hz and $10^{4.8} \Omega$. The maximum voltage of Beam A is 50.2 V, while that of Beam B is 63.1 V.

a stop gap of 3 mm. It is noteworthy that α -IMTPEH and β -IMTPEH encompass devices featuring relatively weak magnetic fields under the large magnet distance of 30 mm, while γ -IMTPEH and δ -IMTPEH entail devices with strong magnetic fields under the small magnet distance of 25 mm. Additionally, the cantilever beams of α -IMTPEH and γ -IMTPEH possess more spacious vibration areas, while the beams in β -IMTPEH and δ -IMTPEH are confined in smaller vibration spaces. In the ensuing section, we will individually explore the power responses of these four configurations. To delve into the influences of the magnet distance, stop gap and load resistance on the power responses of five configurations.

4.1. The conventional linear PEH

To comprehend the influences of the magnet distance and stop gap on the performance of a conventional PEH, the following section undertakes numerical computations of the power and terminal voltage of the system. Fig. 4 visualizes the power spectrum and the terminal voltage of the conventional PEH.

Fig. 4(a) and (b), respectively, show the power responses of Beam A and Beam B in a conventional PEH (without magnets and stoppers) as counterparts for the following comparisons. Beam A attains its peak power of 4.5 mW at the excitation frequency of 8.7 Hz and the external resistance of $10^{5.1} \Omega$. Conversely, Beam B demonstrates a superior maximum power of 17.8 mW at the excitation frequency of 16.3 Hz and the external resistance of $10^{4.8} \Omega$. Fig. 4(c) and (d) depict the terminal voltage profiles of the two beams, indicating their peak values of 35.5 V and 56.3 V around the external resistance of $10^{6.0} \Omega$. Notably, both beams produce voltage responses exclusively within specific narrow frequency ranges: the response of Beam A is confined to the proximity of 11.6 Hz, and the response of Beam B is observed around 16.3 Hz.

The results in Fig. 4 reveal that excluding magnets and stoppers yields two typical cantilever PEHs with conventional linear behavior. Specifically, the power output distribution assumes a characteristic normal curve, showing fluctuations in response to alterations in resistance. This emphasizes the presence of an optimal impedance that maximizes power generation. Notably, the power output proves to be sensitive to variations in the load resistance, culminating in its zenith at the identified optimal impedance point. Additionally, the voltage response displays an ascending trajectory in tandem with increments in

the load resistance. To conclude, removing magnets and stoppers from the configuration engenders prototypical electrical traits reminiscent of a cantilever piezoelectric energy harvester. In this regard, the load resistance notably influences the power output, while the terminal voltage converges to the open circuit voltage.

4.2. IMTPEHs with weak magnetic coupling

Owing to the significant effect of the stop gap on the dynamic motion of the cantilever beam, whether it engages in inter- or intra-well motion greatly influences the power generation of the system. Consequently, this section is dedicated to exploring the effect of the stop gap on the performance in two distinct scenarios: one characterized by a stop gap of 8 mm and the other with 3 mm. By thoroughly analyzing the two scenarios, we can provide insights into how the stop gap affects the electrical characteristics.

Fig. 5 shows the output power and terminal voltage profiles of two piezoelectric patches in the α -IMTPEH configuration. The introduction of the magnet imparts unique vibration responses to both beams, manifesting at two distinct frequencies. One frequency corresponds to the fundamental resonance, whose power performance is called active power (AP), while the other delineates passive responses arising from the influence of magnetic forces called driven power (DP).

In Fig. 5(a), Beam A exhibits the maximum AP of 4.5 mW at the optimal resistance of $10^{5.1} \Omega$ and the excitation frequency of 8.7 Hz. Conversely, the optimal impedance for the DP is $10^{3.8} \Omega$ with the corresponding power of 0.8 mW under the excitation frequency of 15.5 Hz. The maximum AV is 35.5 V at the external resistance of $10^{6.0} \Omega$ in Fig. 5(c), while the DV reaches its highest value of 15.7 V. When Beam A resonates, Beam B experiences forced vibration under the magnetic force and vice versa. This reciprocal influence engenders two discernible response bands in both the power and voltage spectra of both beams. This phenomenon arises from their disparate resonant frequencies (11.6 Hz and 16.3 Hz) and the effect of the magnetic field. This behavior diverges from the standard electrical response of a conventional PEH, thus contributing to the expansion of the power response bandwidth of the energy harvester.

Fig. 5(b) and (d) visualize the power and terminal voltage profiles of Beam B in the α -IMTPEH configuration. Notably, the highest power

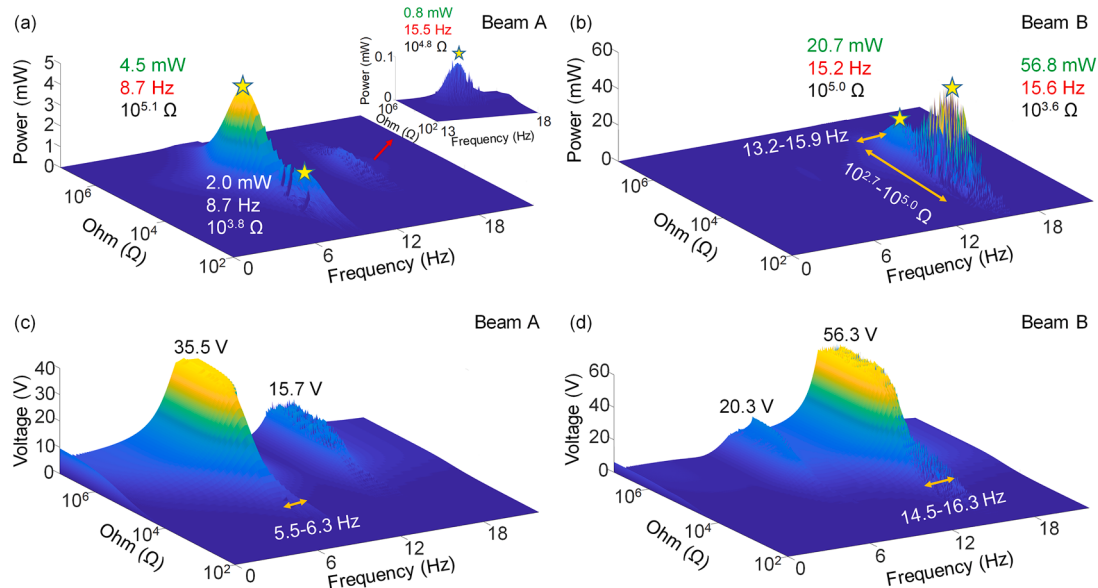


Fig. 5. Numerical results of the power-frequency-resistance responses of (a) Beam A and (b) Beam B and voltage-frequency-resistance responses (c) Beam A and (d) Beam B in α -IMTPEH under the frequency sweep excitation ranging from 0 Hz to 22.0 Hz and the external resistance ranging from $10^{2.0} \Omega$ to $10^{7.0} \Omega$. The maximum power of Beam A is 4.5 mW at 8.7 Hz and $10^{5.1} \Omega$, while that of Beam B is 17.8 mW at 16.3 Hz and $10^{4.8} \Omega$. The maximum terminal voltage of Beam A is 35.5 V, while that of Beam B is 56.3 V.

output of Beam B (56.8 mW) is achieved at the external resistance of $10^{3.6} \Omega$ under the excitation frequency of 15.6 Hz. The power spectrum of Beam B can be categorized into two distinct segments: the AP spans from $10^{2.7} \Omega$ to $10^{5.0} \Omega$. The low resistance power section of the AP demonstrates stronger disorder and nonlinearity. A similar phenomenon is observed in the power response of Beam A, as depicted in Fig. 5(a). The system nonlinear dynamics contributes to elevated voltage and power outputs than a conventional PEH shunted to the same external resistance. However, owing to the interplay of nonlinear terms within the system dynamics, the voltage response of the IMTPEH manifests enhanced disorder and transient characteristics.

To contrast the influence of the stop gap on the electrical performance, Fig. 6 presents the power and voltage responses of the β -IMTPEH configuration. In Fig. 6(a), Beam A attains identical maximum power values of 2.6 mW under two distinct excitation frequencies of 8.4 Hz and 11.9 Hz. The corresponding optimal resistances are the same, $10^{3.9} \Omega$. Remarkably, the instantaneous maximum power of 2.6 mW recorded at the lower load resistance ($10^{3.9} \Omega$) surpasses the corresponding value of 0.8 mW at the higher resistance ($10^{5.1} \Omega$). Upon comparing Fig. 6(a) with Fig. 5(a), a striking distinction is evident: in β -IMTPEH, the optimal resistance of Beam is lower than that in α -IMTPEH. This divergence can be attributed to the interaction between the magnets and stoppers, accentuating the response frequency. This alteration consequently reduces the optimal impedance of the harvester, thereby augmenting the instantaneous power output. By juxtaposing Figs. 4(c), 5(c) and 6(c), a discernible trend becomes apparent. The peak power attained by Beam A of β -IMTPEH surpasses those in α -IMTPEH and the conventional PEH, so is the operational bandwidth (ranging from 5.6 Hz to 11.5 Hz). Fig. 6(c) offers additional insights and reveals that the AV response of Beam A can be divided into two distinct ranges. The first range presents a chaotic distribution spanning from 5.6 Hz to 6.8 Hz, while the subsequent range embodies a linear character over 6.8 Hz - 11.5 Hz. According to the conclusions in the referenced paper [88], the cantilever beam energy harvester, influenced by a magnetic field, undergoes chaotic vibration when exposed to low-frequency excitation. As the excitation frequency increases, the system transits into periodic motion. This transition is explicitly manifested in the voltage response, exhibiting a disordered response under low-frequency excitation and evolving into a periodic response as the frequency increases.

The power response predominantly resides over the AP frequency bandwidth from 12.2 Hz to 17.3 Hz for Beam B of β -IMTPEH in Fig. 6(b), which surpasses the corresponding range observed for Beam B of α -IMTPEH (14.5 Hz - 16.3 Hz). However, the peak power response recorded is lower (40.7 mW vs. 56.8 mW). As shown in Fig. 6(d), the AV frequency range of Beam B extends from 12.2 Hz to 17.3 Hz, with the overall voltage response lower than that of β -IMTPEH. This reduction in voltage amplitude can be attributed to the diminishing deformation of the cantilever beam and piezoelectric patches as the gap between the stoppers decreases.

4.3. IMTPEHs with strong magnetic coupling

The power and voltage responses of the IMTPEH under weak magnetic fields have been explored in Section 4.2. It was found that Beam A consistently generates higher AP than DP. This can be attributed to the fact that, when exposed to weak magnetic fields, the response of Beam A is primarily governed by its resonance, and the influence of magnetic forces remains relatively subdued. However, as the proximity between the two magnets decreases, the magnetic force between them intensifies. In this section, we will delve into the output power and voltage responses of the system in strong magnetic fields.

Fig. 7 illustrates the power and voltage response diagram of the γ -IMTPEH configuration. The AP is generated within the frequency range of 2.2 Hz to 6.1 Hz, occurring alongside a resistance range of $10^{3.0} \Omega$ to $10^{4.2} \Omega$, primarily within the low resistance region, as shown in Fig. 7(a). The power peak, amounting to 6.0 mW, is attained at 5.9 Hz and the external resistance of $10^{3.7} \Omega$. Meanwhile, the DP, influenced by the magnetic effects, falls within 14.2 Hz - 15.2 Hz and the corresponding external resistance range of $10^{3.0} \Omega$ - $10^{3.8} \Omega$. The maximum instantaneous power reaches 92.8 mW at the resistance of $10^{3.7} \Omega$ and the frequency of 15.7 Hz. A comparative analysis between Figs. 7(a) and 5(a) reveals that the peaks of the AP and DP exhibited by Beam A in γ -IMTPEH surpass those in α -IMTPEH (6.0 mW vs. 4.5 mW and 92.8 mW vs. 0.8 mW, respectively). Furthermore, the voltage response characteristics of Beam A are depicted in Fig. 7(c), showing a minor decrease in the AV (33.7 V compared to 35.5 V), an expanded frequency bandwidth (6.5 Hz vs. 0.8 Hz), and a substantial increase in the DV (38.8 V compared to 15.7 V) compared to the α -IMTPEH configuration, as

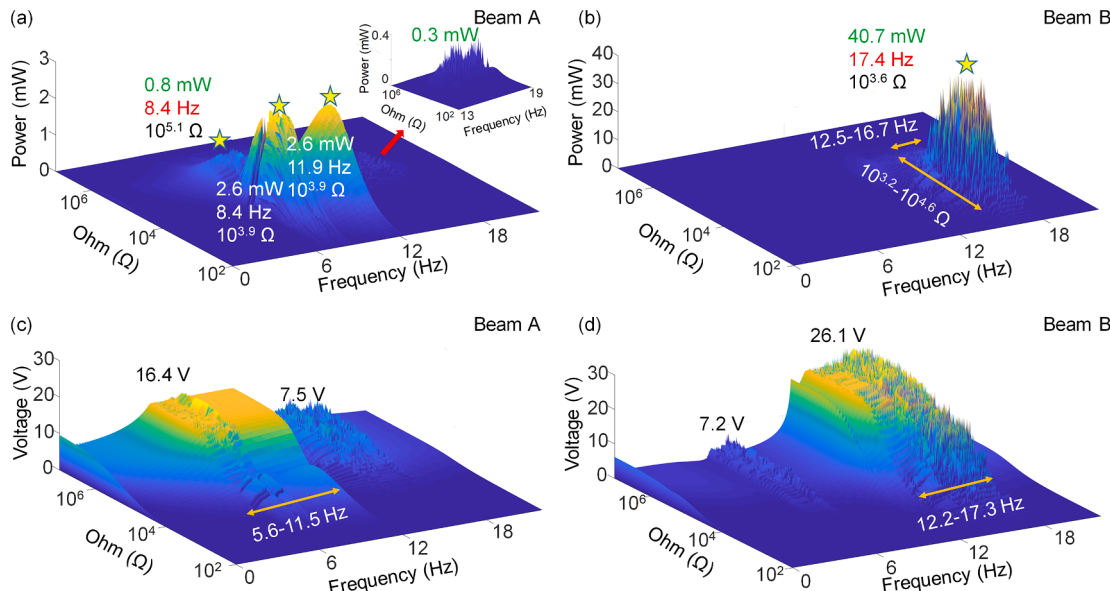


Fig. 6. Numerical results of the power-freq-resistance responses of (a) Beam A and (b) Beam B and voltage-freq-resistance responses of (c) Beam A and (d) Beam B in β -IMTPEH under the frequency sweep excitation ranging from 0 Hz to 22.0 Hz and the external resistance ranging from $10^{2.0} \Omega$ to $10^{7.0} \Omega$. The maximum power of Beam A is 0.8 mW at 8.4 Hz and $10^{3.9} \Omega$, respectively, while that of Beam B is 40.7 mW at 17.4 Hz and $10^{3.6} \Omega$. The maximum terminal voltage of Beam A is 16.4 V, while that of Beam B is 26.1 V.

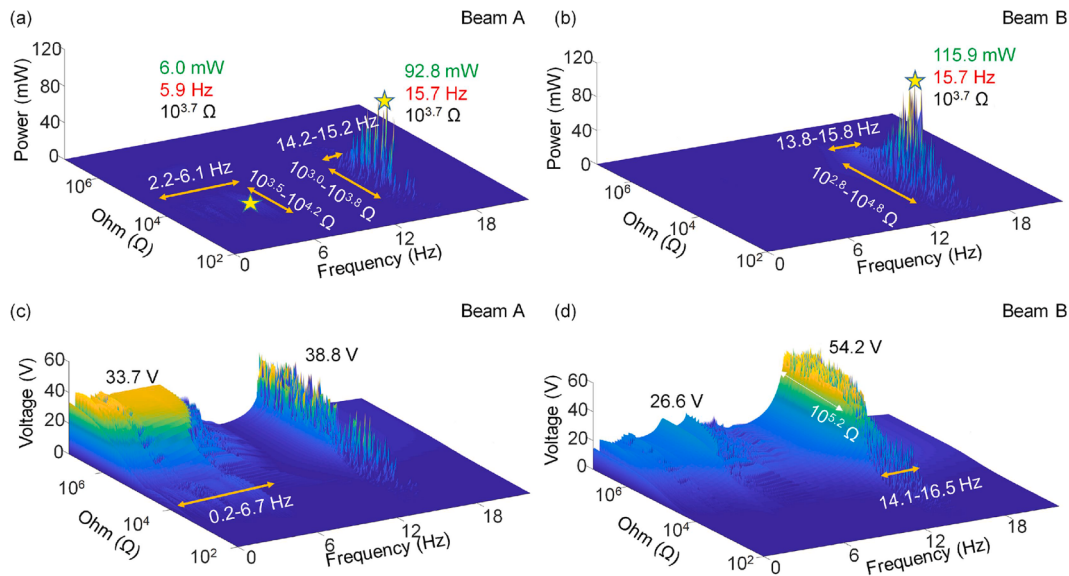


Fig. 7. Numerical results of the power-frequency-resistance responses of (a) Beam A and (b) Beam B and voltage-frequency-resistance responses of (c) Beam A and (d) Beam B in γ -IMTPEH under the frequency sweep excitation ranging from 0 Hz to 22.0 Hz and the external resistance ranging from $10^{2.0} \Omega$ to $10^{7.0} \Omega$. The maximum power of Beam A is 92.8 mW at 15.7 Hz and $10^{3.7} \Omega$, while that of Beam B is 115.9 mW at 15.7 Hz and $10^{3.7} \Omega$. The maximum terminal voltage of Beam A is 38.8 V, while that of Beam B is 54.2 V.

depicted in Fig. 5(c).

Comparing Figs. 7(b) and 5(b) shows that the AP (115.9 mW) demonstrated by Beam B in γ -IMTPEH surpasses that (56.8 mW) in α -IMTPEH. Moreover, the response frequency bandwidth of γ -IMTPEH (2.0 Hz) is narrower than that of the α -IMTPEH configuration (2.7 Hz), with the resistance range experiencing only minor changes ($10^{2.8} \Omega$ - $10^{4.8} \Omega$ for γ -IMTPEH versus $10^{2.7} \Omega$ - $10^{5.0} \Omega$ for α -IMTPEH). Although the voltages produced by Beam B of γ -IMTPEH are smaller than those of α -IMTPEH (e.g., 14.4 V for γ -IMTPEH versus 35.5 V for α -IMTPEH), the voltage frequency bandwidth of γ -IMTPEH is wider (2.4 Hz for γ -IMTPEH versus 1.8 Hz for α -IMTPEH) when comparing Figs. 7(d) and 5(d). This is because the smaller magnet distance results in augmented potential energy of the system, which intensify the magnetic force between the two magnets. Consequently, the DP/DV surpass the AP/AV for

Beam A. Additionally, due to the incremental strengthening effect brought by the magnetic field on the cantilever beam, both the power and voltage response frequency bandwidths are widened.

Fig. 8(a) shows the AP profile of Beam A in the δ -IMTPEH configuration. The AP occurs over 2.5 Hz to 5.8 Hz and corresponds to the resistance range from $10^{3.0} \Omega$ to $10^{4.2} \Omega$. The maximum instantaneous power is 5.0 mW observed at the frequency of 5.6 Hz and the resistance of $10^{3.7} \Omega$. A comparative analysis of the DP bandwidth of Beam A in δ -IMTPEH (11.5 Hz - 20.1 Hz) with that of γ -IMTPEH (14.2 Hz - 15.2 Hz) underscores a broader bandwidth of δ -IMTPEH while a lower peak power (38.2 mW) than that of γ -IMTPEH (92.8 mW). Turning attention to the findings in Figs. 8(c) and 7(c), the AV response (peak voltage of 14.4 V) of Beam A in δ -IMTPEH is smaller than that in γ -IMTPEH (33.7 V). The presence of stop blocks limits the movement space and restricts

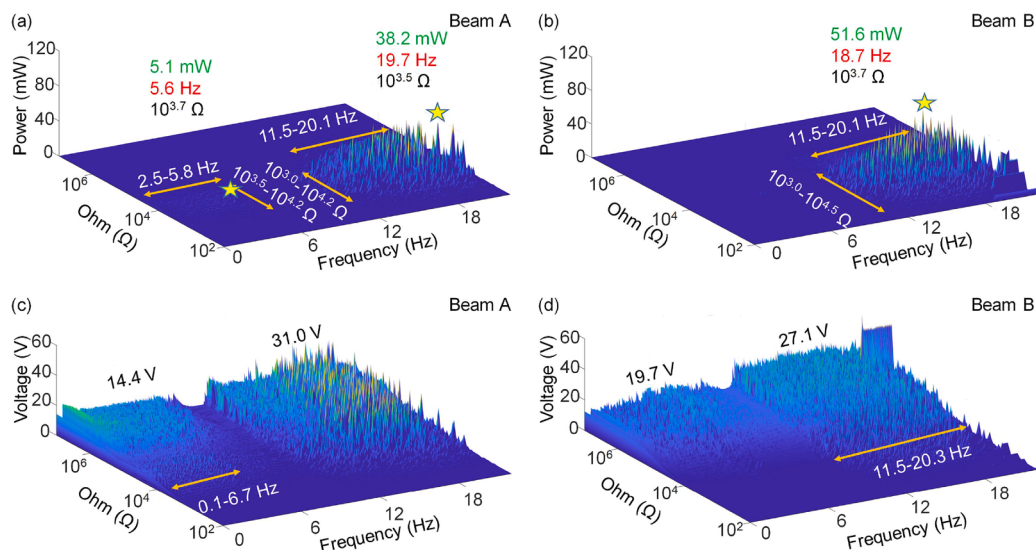


Fig. 8. Numerical results of the power-frequency-resistance responses of (a) Beam A and (b) Beam B and voltage-frequency-resistance responses of (c) Beam A and (d) Beam B in δ -IMTPEH under the frequency sweep excitation ranging from 0 Hz to 22.0 Hz and the external resistance ranging from $10^{2.0} \Omega$ to $10^{7.0} \Omega$. The maximum power of Beam A is 38.2 mW at 19.7 Hz and $10^{3.5} \Omega$, while that of Beam B is 51.6 mW at 18.7 Hz and $10^{3.7} \Omega$. The maximum terminal voltage of Beam A is 31.0 V, while that of Beam B is 27.1 V.

the beam deformation. This scenario compels the cantilever beam to sustain continuous motion on a high potential energy orbit, fostering a disordered voltage response across the system. Diverging from the power response of γ -IMTPEH, the DP and the corresponding bandwidth of δ -IMTPEH exceed those of the AP. This can be explained by the increased magnetic field forces exerted upon the two beams of δ -IMTPEH compared to γ -IMTPEH.

As demonstrated in Fig. 8(b), the AP peak of Beam B in δ -IMTPEH appears at 18.7 Hz and $10^{3.8} \Omega$. This peak is situated over 11.5 Hz - 20.1 Hz, with a resistance range from $10^{3.0} \Omega$ to $10^{4.5} \Omega$. A direct comparison between Figs. 8(b) and 7(b) shows that the AP peak (51.6 mW) for Beam B in δ -IMTPEH is smaller than that achieved in γ -IMTPEH (115.9 mW). Furthermore, the truncation frequency bandwidth of δ -IMTPEH (8.6 Hz) exceeds that of γ -IMTPEH (2.0 Hz). Similarly, upon contrasting Figs. 8(d) and 7(d), the peak voltage of δ -IMTPEH (27.1 V) is smaller than that of γ -IMTPEH (54.2 V). Reducing the stop gap under the influence of a strong magnetic field curtails the available motion space for the cantilever beam, which restricts the beam deformation and the stains in the associated piezoelectric element. Furthermore, the intensified hardening effect induced by collisions at a smaller stop gap engenders a more pronounced impact resulting in a broader bandwidth of the system. Comparing Figs. 8(b) and 6(b), the AP peak of Beam B in δ -IMTPEH (55.0 mW) surpasses that in β -IMTPEH (40.7 mW). Correspondingly, the frequency bandwidth of δ -IMTPEH exceeds that of β -IMTPEH, while the impedance range remains similar ($10^{3.0} \Omega$ - $10^{4.5} \Omega$ for δ -IMTPEH versus $10^{3.2} \Omega$ - $10^{4.6} \Omega$ for β -IMTPEH). Furthermore, comparing Fig. 8(d) and Fig. 6(d), the peaks of the AV and DV of Beam B in δ -IMTPEH (19.7 V and 27.1 V) beat those in β -IMTPEH (7.2 V and 26.1 V). The voltage bandwidths of δ -IMTPEH (6.6 Hz and 8.8 Hz) are also broader than those of β -IMTPEH (5.9 Hz and 5.1 Hz).

5. Experimental validation

The electromechanical coupling model of the system was established in Section 2, and the main factors affecting the output performance of the system, such as the magnet distance and the stop gap, were discussed in Section 4. This section validates the numerical calculation results

through frequency sweep, fixed frequency voltage response, and power response.

This section will experimentally validate the numerical results obtained in Sections 3 and 4, focusing on terminal voltage and power responses. Fig. 9 shows the experimental setup. The computer software generates excitation waveforms to the power amplifier (Econ. E5874A), which amplifies and transmits the control signals to the vibration shaker (Econ. E-JZK-50) through the power supply, inputting forced vibration to the prototype. The prototype is mounted on a base structure attached to the vibration shaker, with its beams parallel to the direction of gravity to minimize the gravity influence. Two cantilever beams with magnets at their free ends are positioned face to face and clamped on the base. Piezoelectric patches are partially attached to the upper surfaces of the beams. Thick aluminum plates are used as stoppers, placed above and below the magnets, and securely fixed on the vertical plates. When the piezoelectric patches deform with the cantilever beams, the displacements of ions within the patches result in a change in electric dipole moment and the generation of an electric field. The IMTPEH prototype is excited by a vibration shaker. The input excitation is set in two modes: a fixed frequency excitation at the frequency of 14.0 Hz and a sweep frequency excitation at the frequency sweeping rate of 10 Hz/min ranging from 4.0 Hz to 22.0 Hz with an acceleration of 0.6 g (1 g = 9.8 m/s²). The output voltages of the two piezoelectric patches attached to the beams are measured using an oscilloscope (Tektronix MDO3024).

5.1. Validation of the terminal voltage under constant frequency excitation

According to [34–36] and Eq. (22), the matching impedance of a PEH is related to its internal capacitance and response frequency.

$$R_o = \frac{1}{2\pi f_n C} \quad (23)$$

where R_o is the matching impedance, f_n is the response frequency of the piezoelectric patch, and C is the internal capacitance of the piezoelectric patch. In Fig. 4, the natural frequencies of both beams without the

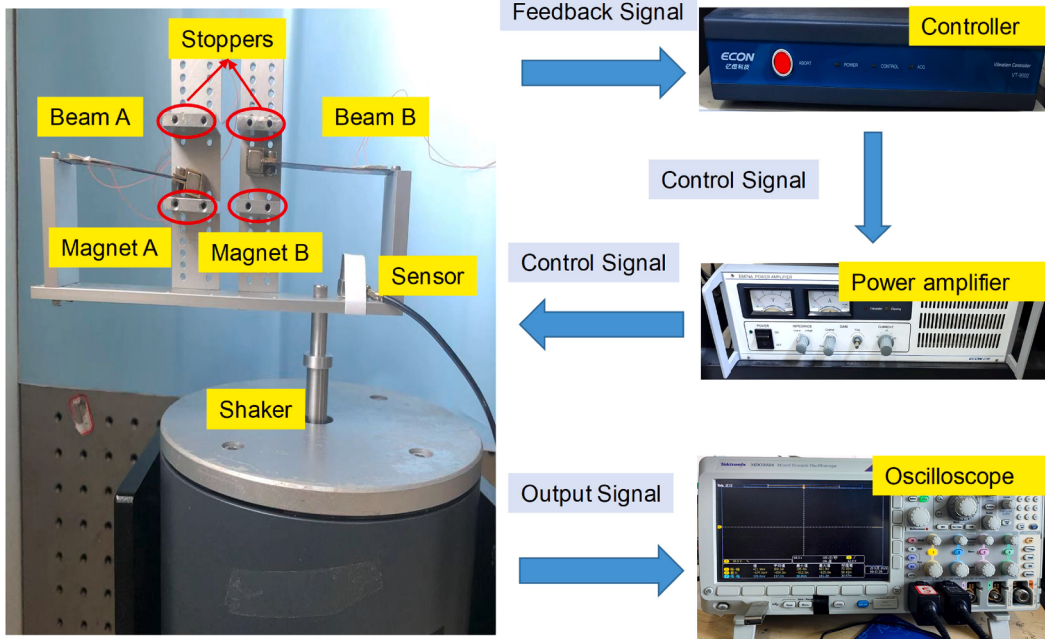


Fig. 9. Electrodynamic shaker platform for the vibration test. It consists of an electrodynamic shaker, a power amplifier, a controller, an oscilloscope, and an accelerometer. The IMVPEH is installed on the shaker. The acceleration signals are fed back to the controller, whose control signals are amplified by the amplifier and transmitted to the shaker. The electrical signals are measured by the oscilloscope.

magnetic coupling are 11.6 Hz and 16.3 Hz. According to Eq. (23), the calculation results of the internal resistance of two piezoelectric beams are $10^{5.0} \Omega$ and $10^{4.8} \Omega$, which are equal to their matching impedance calculated in Fig. 4. Due to the effect of collisions, the response frequency of the piezoelectric beam increases, thereby reducing its internal resistance according to Eq. (23). This also results in a decrease or expansion of the matching impedance of the energy harvester, thereby increasing the response power. To provide a more detailed description of the effect of the collision on the matching impedance, this section will present the simulation and experimental results of the terminal voltage generated by the four IMTPEHs at 14.0 Hz and 0.6 g, with a shunted resistor of $10^{7.0} \Omega$. In Fig. 10, the solid red lines represent the experimental results of Beam A and Beam B, respectively, while the dashed blue lines are the numerical results.

As shown in Fig. 10, the voltage waveforms obtained by numerical simulation roughly agree with the experimental results. The voltage amplitude discrepancy is within 10 %. In Fig. 10(a), the experimental results indicate that response frequency of Beam A is 7.0 Hz by forced vibration, and there is almost no high-frequency component by collision. According to Eq. (23), its corresponding power is relatively low. The experimental voltage response of Beam B contains a 555.5 Hz high-frequency component by collision, corresponding to an optimal impedance of $10^{3.3} \Omega$, while the simulation value is 101.0 Hz and $10^{4.0} \Omega$. This deviation may partly arise from the limitation of the dynamic model, which only considers the first three vibration modes of the cantilever beam and the segmented linear collision model. The third-order mode of the cantilever beam used in the model has a response frequency within 500.0 Hz, which makes it difficult for the system to respond to the high-order frequency generated by the collision.

In Fig. 10(b), experimental results of Beam A exhibit a collision response at 120.0 Hz. The corresponding optimal impedance is $10^{3.9} \Omega$. The simulation results for Beam A lack an evident high-frequency component. Moving onto the experimental results for Beam B in Fig. 10(b), one notes a collision frequency of 500.0 Hz, associated with a matching impedance of $10^{3.3} \Omega$. Additionally, the collision frequency calculated is 101.0 Hz, corresponding to a matching impedance of $10^{4.0} \Omega$, which is close to the matching impedance of $10^{3.6} \Omega$ in Fig. 6(b). This difference in matching impedances is because only the low-frequency components are considered in the dynamic model, which causes an increase in the corresponding matching impedance, as indicated by Eq.

(23).

In Fig. 10(c), the collision frequency in the experimental results of Beam A is 166.7 Hz, indicating a matching impedance of approximately $10^{3.8} \Omega$. However, in the numerical voltage results, the high-frequency response occurs at 74.0 Hz, corresponding to a matching impedance of $10^{4.1} \Omega$, which is slightly higher than the experimental result. This discrepancy indicates that the numerical simulation cannot accurately predict the exact matching impedance observed in the experiment. Furthermore, the high-frequency component in the simulation results of Beam B is lower than that identified in the experimental results, implying an overestimation of the matching impedance.

In Fig. 10(d), both the experimental and numerical results of Beam A exhibit a collision frequency of 166.7 Hz, corresponding to a matching impedance of approximately $10^{3.8} \Omega$. This value agrees with the optimal impedance ($10^{3.7} \Omega$) observed in Fig. 8(a). Due to the limitations imposed by the stopper, Beam A in δ -IMTPEH experiences high-energy orbit vibration under the dual-hardening effect of magnetic force and collision. As a result, Beam A vibrates at the same frequency as Beam B, which is different from the first three configurations. In the first three harvesters, the weaker hardening effect on Beam A caused by magnetic fields and collisions leads to a response frequency that is half that of Beam B. In the experimental results of Beam B, a collision frequency of 1000.0 Hz is observed. The numerical results show a collision frequency of 400.0 Hz. The experimental and numerical results correspond to matching impedances of $10^{3.0} \Omega$ and $10^{3.4} \Omega$, respectively. We can use the same theory to explain the discrepancy: the numerical model only accounts for lower-order vibration modes, resulting in a reduced collision response.

In conclusion, the numerical calculations considered only the first three order modes of the cantilever beam, resulting in a lower collision response frequency than the experimental results. Consequently, the matching impedances predicted by numerical simulations are slightly higher than experimental results. Nonetheless, it is worth noting that the differences between numerically predicted matching impedances and experimental ones fall within an acceptable range.

5.2. Validation of the terminal voltage under the sweep frequency excitation

The preceding section validated the response waveform and

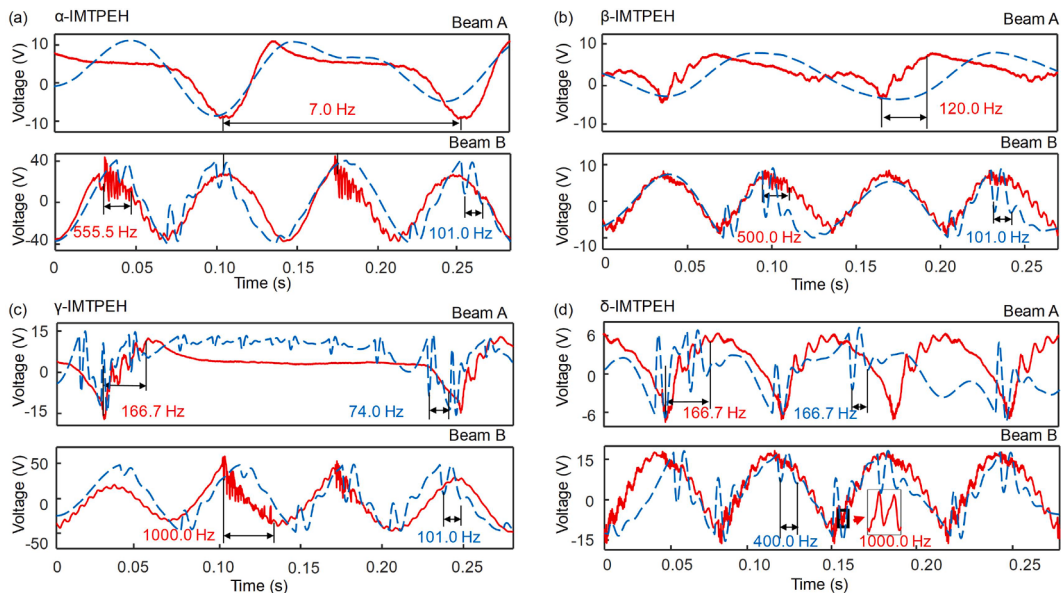


Fig. 10. Comparison of the experimental and simulation results of the terminal voltage responses generated by the four IMTPEHs under the excitation frequency of 16.0 Hz and the acceleration of 0.6 g. The voltage responses of Beam A and Beam B in (a) α -IMTPEH, (b) β -IMTPEH, (c) γ -IMTPEH, (d) δ -IMTPEH. The red solid line represents the experimental results, while the blue dashed line represents the numerical results.

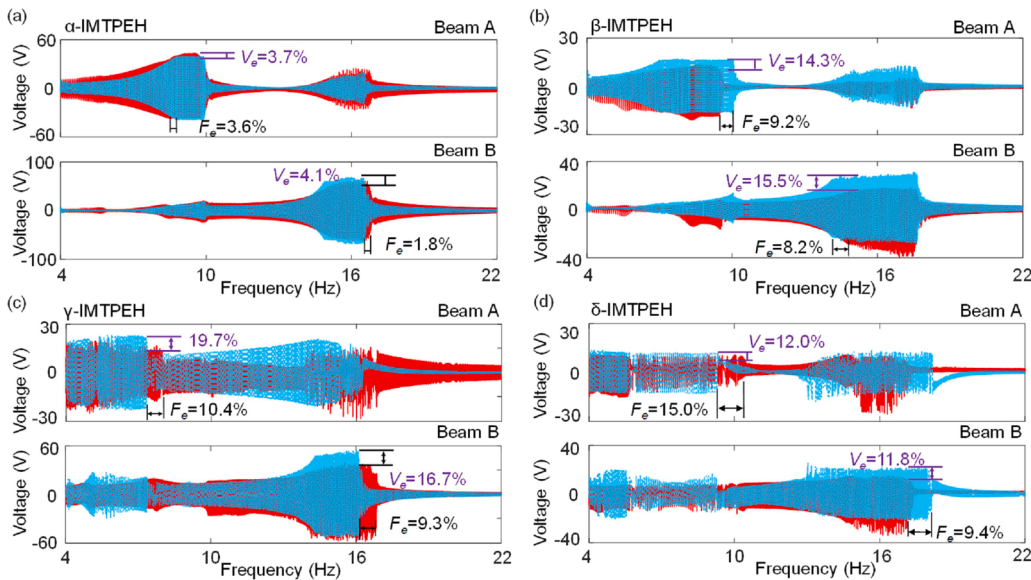


Fig. 11. Comparison of the experimental and simulation results of the voltage responses generated by the four IMTPEHs under frequency sweep excitation ranging from 4.0 Hz to 22.0 Hz and the acceleration of 0.6 g. The voltage responses of Beam A and Beam B in (a) α -IMTPEH, (b) β -IMTPEH, (c) γ -IMTPEH, (d) δ -IMTPEH. The red line represents the experimental results, while the blue line represents the numerical results.

matching impedance of the energy harvester. This section aims to further validate the frequency bandwidths by conducting frequency sweep experiments. Fig. 11 shows the voltage-frequency responses of the four harvesters subjected to an upward frequency sweep excitation from 4.0 Hz to 22.0 Hz and a constant acceleration of 0.6 g. The blue dashed lines represent the numerical results obtained by solving Eqs. (18) and (19). The resistance was set to $10^{7.0} \Omega$. The red solid lines represent the experimental results obtained under open circuit conditions. The geometric and material parameters of the experimental prototype and numerical model are listed in Table 1.

To facilitate the representation of errors between numerical and experimental results, we employ the absolute voltage error percentage (V_e) and the absolute collision bandwidth error percentage (F_e) as error metrics. Specifically, V_e is defined as $V_e = |V_{\text{experimental}} - V_{\text{numerical}}| / V_{\text{experimental}} \times 100\%$, where $V_{\text{experimental}}$ and $V_{\text{numerical}}$ denote the experimental and numerical voltage, respectively; F_e is defined as $F_e = |F_{\text{experimental}} - F_{\text{numerical}}| / F_{\text{experimental}} \times 100\%$, where $F_{\text{experimental}}$ and $F_{\text{numerical}}$ denote the experimental and numerical frequency bandwidth, respectively.

As shown in Fig. 11, regarding the peak voltage, the errors of the numerical results of the AV for Beam A in the four harvesters are 3.7 %, 14.3 %, 19.7 %, and 12.0 %, respectively. Similarly, for Beam B, the numerical errors of the AV are 4.1 %, 15.5 %, 16.7 %, and 11.8 %, respectively. All these errors fall below an acceptable threshold of 20 %. Regarding the frequency bandwidth prediction, the numerical errors of the AV for Beam A in the four harvesters are 3.6 %, 9.2 %, 10.4 %, and 15.0 %, respectively. For Beam B, the errors are 1.8 %, 8.2 %, 9.3 %, and 9.4 %, respectively. Comparatively, the bandwidth errors for γ -IMTPEH and δ -IMTPEH are greater than those for α -IMTPEH and β -IMTPEH, indicating that the prediction error under strong magnetic field conditions is more significant than that under weak magnetic field conditions. The presented model uses the point dipole model [34] to predict the magnetic force, which simplifies the magnets as particles. However, magnets have specific volumes that affect the magnetic field distributions in practice.

Compared with Fig. 11(a), (c) and 11(b), (d), there is a wider cutoff frequency bandwidth for small stop gaps. Similarly, compared to α -IMTPEH, β -IMTPEH and γ -IMTPEH, δ -IMTPEH, a small magnet distance also results in a wider response frequency band. Both small stop gap and magnet distance will harden the cantilever beam, thereby

enhancing the nonlinear stiffness of the system.

5.3. Experimental verification of power response

The numerical findings presented in Section 4 unveiled the influence of the magnet distance and the stopper position on the power response of the IMTPEH. Specifically, as the magnet distance and the stop gap decrease, the power response exhibits wider a frequency bandwidth. In this section, we aim to validate the numerical results through frequency sweep experiments, using the parameters listed in Table 1. Two resistors were connected to two piezoelectric patches on the beams through wires, and the voltage across the resistors were measured through an oscilloscope simultaneously. The resistance of $10^3 \Omega$, $10^{3.3} \Omega$, $10^{3.6} \Omega$, $10^{3.8} \Omega$, $10^{3.9} \Omega$, $10^{4.0} \Omega$, $10^{4.3} \Omega$, $10^{4.6} \Omega$, $10^{4.8} \Omega$, $10^{4.9} \Omega$, $10^{5.0} \Omega$, $10^{6.0} \Omega$ and $10^{7.0} \Omega$ was selected. The power generated by the piezoelectric unit in the resistance were calculated using Eq. (21). The frequency range of the sweep excitation is 0 Hz - 22.0 Hz, and the excitation acceleration is 0.6 g.

Fig. 12 illustrates the power and voltage responses of α -IMTPEH under the above external resistance and excitation frequency ranging from 4.0 Hz to 22.0 Hz with a constant acceleration of 0.6 g. In Fig. 12 (a), the maximum AP of Beam A is 3.6 mW with a resonant frequency of 8.3 Hz and a matching resistance of $10^{3.8} \Omega$. The maximum DP is 0.025 mW, achieved at 16.1 Hz and a matching resistance of $10^{3.6} \Omega$. As observed in Fig. 12(b), the maximum AP is 240.4 mW occurring at the frequency of 15.1 Hz and a matching resistance of $10^{3.8} \Omega$. These findings align with the AP in the numerical results in Fig. 5(b). Compared to the conventional linear PEH in Fig. 5, the output power of Beam B in α -IMTPEH has been significantly improved, and the response frequency band (power greater than 17.8 mW corresponding to the maximum power of the linear PEH) is 13.3 Hz - 15.7 Hz with a response power range of $10^{3.0} - 10^{4.3} \Omega$. This method expands the response frequency bandwidth and matching impedance range compared to traditional piezoelectric cantilever beams.

Fig. 12(c) shows that the maximum AV produced by Beam A is 22.5 V at 8.3 Hz when shunted to the resistance of $10^{7.0} \Omega$. The maximum DV is 14.9 V, produced at 15.1 Hz. Similarly, Fig. 12(d) demonstrates that the maximum AV of Beam B is 48.7 V at 15.1 Hz, and the maximum DV is 22.0 V at 8.7 Hz. The experimentally observed terminal voltage trends match the theoretical predictions in Fig. 5(c) and (d). However, the

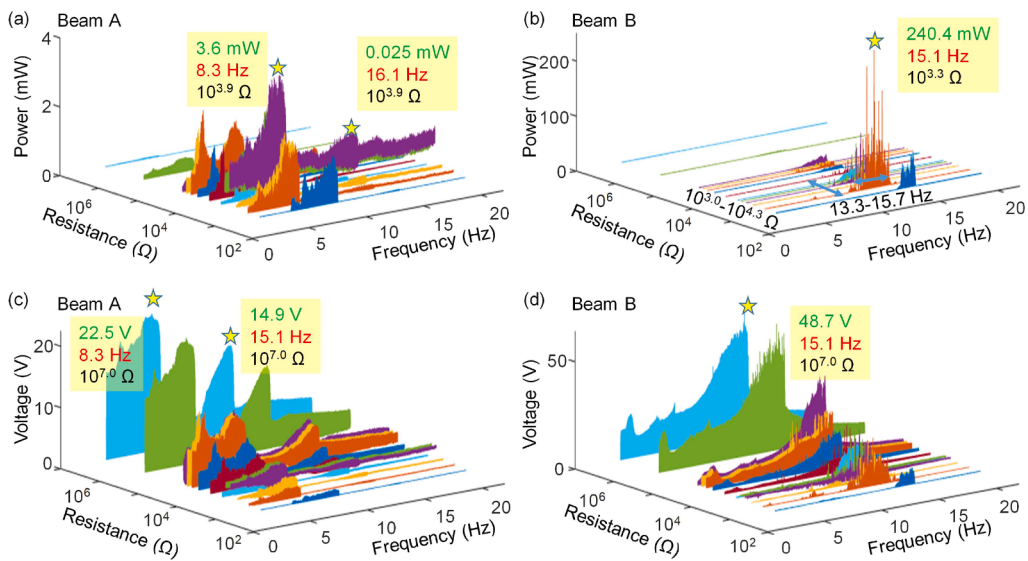


Fig. 12. Experimental results of the power-frequency-resistance responses of (a) Beam A, (b) Beam B, and the voltage-frequency-resistance responses of (c) Beam A, (d) Beam B in α -IMTPEH under frequency sweep excitation ranging from 4.0 Hz to 22.0 Hz and the acceleration of 0.6 g. The corresponding external resistance values, in ascending order, are $10^3 \Omega$, $10^{3.3} \Omega$, $10^{3.6} \Omega$, $10^{3.8} \Omega$, $10^{3.9} \Omega$, $10^{4.0} \Omega$, $10^{4.3} \Omega$, $10^{4.6} \Omega$, $10^{4.8} \Omega$, $10^{4.9} \Omega$, $10^{5.0} \Omega$, $10^{6.0} \Omega$ and $10^{7.0} \Omega$. The yellow pentagram represents the local/global maximum response power in Fig. 12(a) and (b) and local/global maximum response voltage in Fig. 12(c) and (d).

experimental voltage values are slightly lower than the theoretical predictions. The piezoelectric patch was bonded to the cantilever beam using glue in the experiment, which introduced a certain buffering effect for the piezoelectric patch and reduced the actual electromechanical coupling coefficient of the system.

Fig. 13 presents the power responses of β -IMTPEH, γ -IMTPEH and δ -IMTPEH. Fig. 13(a.1) shows that the maximum AP of β -IMTPEH is 1.1 mW at $10^{3.0} \Omega$ and 5.3 Hz, while the maximum DP is 0.8 mW at $10^{3.0} \Omega$ and 15.5 Hz. Similar to the numerical power responses in Fig. 6(a), the experimental results also exhibit the AP/DP. Fig. 13(a.2) shows that the power response of Beam B spans from 7.7 Hz to 15.3 Hz, with the resistance ranging from $10^{3.0} \Omega$ to $10^{4.8} \Omega$ and a peak of 20.1 mW at 15.3 Hz and $10^{3.0} \Omega$. When compared with the numerical results in Fig. 6(b),

the peak amplitude in the experimental results decreases, but the frequency bandwidth widens. Compared to α -IMTPEH, the response frequency and matching impedance range of β -IMTPEH are wider, but the power response peak is lower. The stop block restricts the deformation of the cantilever beams, thereby reducing the output amplitude of the piezoelectric unit. However, the collision causes the frequency bandwidth to widen, thereby expanding the impedance matching range and response frequency.

In particular, Beam A in γ -IMTPEH attains its pinnacle of the AP at 4.0 mW, 6.3 Hz and $10^{3.6} \Omega$. Contrarily, its zenith of the DP manifestation peaks at 7.8 mW, 14.6 Hz and $10^{3.6} \Omega$, as evidenced in Fig. 13 (b.1), which spans the frequency spectrum from 11.1 Hz to 14.9 Hz and a parallel range of the resistance between $10^{3.0} \Omega$ and $10^{4.3} \Omega$.

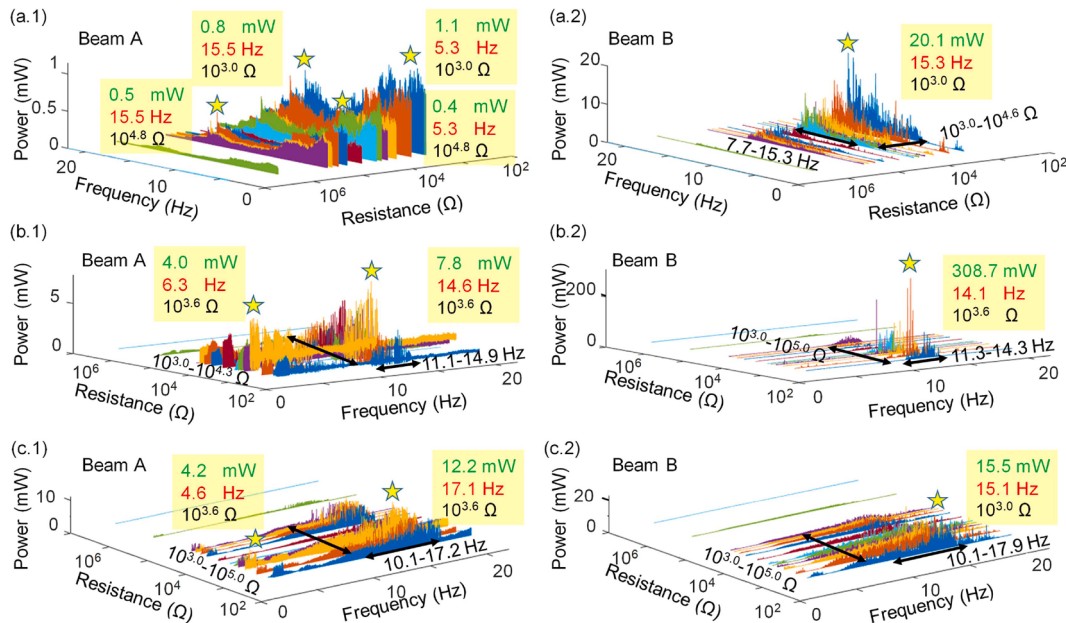


Fig. 13. Experimental results of the power-frequency-resistance responses of (a) β -IMTPEH, (b) γ -IMTPEH, (c) δ -IMTPEH under frequency sweep excitation ranging from 4.0 Hz to 22.0 Hz and the acceleration of 0.6 g. The corresponding external resistance values, in ascending order, are $10^3 \Omega$, $10^{3.3} \Omega$, $10^{3.6} \Omega$, $10^{3.8} \Omega$, $10^{3.9} \Omega$, $10^{4.0} \Omega$, $10^{4.3} \Omega$, $10^{4.6} \Omega$, $10^{4.8} \Omega$, $10^{4.9} \Omega$, $10^{5.0} \Omega$, $10^{6.0} \Omega$ and $10^{7.0} \Omega$. The yellow pentagram represents the local/global maximum response power.

Analogously, the apogee of Beam B in the AP materializes at 308.7 mW, synchronized with the frequency of 14.1 Hz and $10^{3.6} \Omega$ within the frequency range of 11.3 Hz to 14.3 Hz, coupled with the resistance span of $10^{3.0} \Omega$ to $10^{5.0} \Omega$, as depicted in Fig. 13(b.2). Comparing γ -IMTPEH and α -IMTPEH, the closer magnetic distance result in a higher potential energy of the cantilever beam, leading to higher collision frequencies. Similar to α -IMTPEH, the cantilever beam in γ -IMTPEH has a wider vibration space than β -IMTPEH, allowing the piezoelectric patches to deform more fully, resulting in a higher power output from the piezoelectric patch.

In Fig. 13(c.1), the AP peak of Beam A in δ -IMTPEH is 4.2 mW, occurring at 4.6 Hz and $10^{3.6} \Omega$. And the DP peak is 12.2 mW, observed at 17.1 Hz and $10^{3.6} \Omega$. The DP falls within the power response region from 10.1 Hz to 17.2 Hz, and the resistance spans from $10^{3.0} \Omega$ to $10^{5.0} \Omega$. Moving on to Fig. 13(c.2), the AP peak is 15.5 mW, appearing at 15.1 Hz and $10^{3.0} \Omega$. This power peak is produced within the frequency range of 10.1 Hz - 17.9 Hz and the resistance range of $10^{3.0} \Omega$ to $10^{5.0} \Omega$. Compared to the first three cases, δ -IMTPEH has the widest response frequency band and impedance range. The narrow stop space prevents the beams in δ -IMTPEH from moving to the static equilibrium position, therefore the cantilever beams are always at a higher potential energy, resulting in wideband high-frequency collisions on high-energy orbits. Although the compact space limits the peak output of the system, it expands the adaptability range of the system. The power of Beam B is higher than that of Beam A, which is due to a higher collision frequency of Beam B shown in Fig. 9, resulting in lower internal resistance of the patches.

Comparing the four configurations, as the structure becomes more compact, the output power of the system decreases, but the response frequency band and matching impedance range broaden. Compared to the conventional PEH, the IMTPEH has higher output power, wider response frequency band and matching impedance range, and can better adapt to different excitation frequencies and installation spaces in practical application scenarios.

Through a comprehensive comparison of experimental and numerical results, the voltage and power responses in the experimental data are generally consistent with the numerical predictions regarding the primary response characteristics. Some differences between the two results are caused by many practical factors, such as manufacturing error induced non-ideal distances between magnets and stoppers. Despite these imperfections in the experimental prototype, the main response characteristics are well-reflected in both the experimental and numerical results. Despite the errors, the electromechanical model developed in this study provides a solid foundation for conducting structure design and investigating the performance of the energy harvester for real-world applications.

6. Conclusions

In this paper, an IMTPEH has been proposed to enhance the output performance of PEHs in a compact space. In the IMTPEH, two cantilever beams were coupled by leveraging magnetic interaction to achieve a wide response frequency bandwidth, and stoppers were introduced to limit the motion amplitude of the beams and provide collisions between magnets and stoppers, which significantly increased the response frequency of the cantilever beams.

The electromechanical governing equations was established based on the Hamilton's principle and the Galerkin method. The first third

order modes of the cantilever beams were applied for numerical calculation. Based on these equations, numerical results of the static potential energy and open circuit voltage of the system were obtained. Both reducing the magnet distance and increasing the stiffness ratio of the two cantilever beams can increase the total potential energy and the frequency bandwidth of the voltage response, which also can be achieved by increasing the external acceleration and decreasing the stop gap. The power and voltage responses varying with the excitation frequency and external resistance of four types of IMTPEHs with different magnet distances and stop gaps have been studied based on numerical results. Compared to Beam B, Beam A is more likely to exhibit two stages of power and voltage responses, with AP/DP and AV/DV being more pronounced, while Beam B has higher power and voltage peaks. Compared to traditional cantilever beams, both beams in the four configurations exhibit a wider response frequency bandwidth, matching impedance range, and higher response power, e.g. the power peaks of Beam B in γ -IMTPEH is 117.9 mW, which is 6.5 times that of the conventional Beam B.

The results of the frequency fixed and sweep experiments generally agree with the simulation results in voltage and power. In the experiment, the collisions between magnets and stoppers caused the piezoelectric patches to generate high frequency voltage responses of 500.0 Hz - 1000.0 Hz, which significantly reduced their internal resistance and thus increased the power. Comparing the power outputs of the four structures, the maximum power output is 308.7 mW from Beam B in γ -IMTPEH at 14.1 Hz and $10^{3.6} \Omega$, while the widest response frequency bandwidth and impedance matching range are 10.1 Hz - 17.9 Hz and $10^{3.0} \Omega$ - $10^{5.0} \Omega$ from Beam B in δ -IMTPEH. The IMTPEH improves the potential for PEHs in practical applications, especially in compact spaces.

CRediT authorship contribution statement

Li Zhao: Writing – original draft, Data curation, Conceptualization. **Guobiao Hu:** Writing – review & editing. **Shengxi Zhou:** Visualization, Validation. **Yan Peng:** Investigation, Funding acquisition. **Shaorong Xie:** Supervision. **Zhongjie Li:** Project administration, Methodology.

Declaration of competing interest

The authors declare the following financial interests/personal relationships which may be considered as potential competing interests: Zhongjie Li reports financial support was provided by the National Natural Science Foundation of China. Zhongjie Li reports financial support was provided by the Shanghai Science and Technology Committee. Yan Peng reports financial support was provided by the National Natural Science Foundation of China.

Data availability

Data will be made available on request.

Acknowledgments

This work was funded by the National Natural Science Foundation of China (No. 62225308; No. 62001281) and the Shanghai Science and Technology Committee (No.:22dz1204300).

Appendix A

Due to the geometric and material change of the piezoelectric beam, the shape function $\phi(x)$ is divided into two components as follows:

$$\phi_{ij1}(x) = C_{ij1}\cos\beta_{ij1}x + C_{ij2}\cosh\beta_{ij1}x + C_{ij3}\sin\beta_{ij1}x + C_{ij4}\sinh\beta_{ij1}x, \quad (A1)$$

$$\phi_{ij2}(x) = D_{ij1}\cos\beta_{ij2}x + D_{ij2}\cosh\beta_{ij2}x + D_{ij3}\sin\beta_{ij2}x + D_{ij4}\sinh\beta_{ij2}x, \quad (\text{A2})$$

where C_{ijk} , D_{ijk} , β_{ij1} and β_{ij2} are unknown constants to be determined, and $k = 1, 2, 3, 4$.

The boundary and compatibility conditions of the modal shape functions $\phi_{ijn}(x)$ are given as follows:

$$\phi_{ij1}(0) = 0, \dot{\phi}_{ij1}(0) = 0 \text{ at } x = 0, \quad (\text{A3})$$

$$\phi_{ij1}(L_{Pi}) = \phi_{ij2}(L_{Pi}), \dot{\phi}_{ij1}(L_{Pi}) = \dot{\phi}_{ij2}(L_{Pi})$$

$$E_{Ci}I_{Ci}\phi''_{ij1}(L_{Pi}) = E_{Bi}I_{Bi}\phi''_{ij2}(L_{Pi}), E_{Pi}I_{Pi}\phi''_{ij1}(L_{Pi}) = E_{Bi}I_{Bi}\phi''_{ij2}(L_{Pi}) \text{ at } x = L_{Pi}, \quad (\text{A4})$$

$$\left. \begin{aligned} E_{Bi}I_{Bi}\phi''_{ij2}(L_{Pi} + L_{Bi}) &= (I_{Bi} + m_{Mi}d_{Mi}^2)\omega_{ij}^2\phi'_{ij2}(L_{Pi} + L_{Bi}) + m_{Mi}d_i\omega_{ij}^2\phi_{ij2}(L_{Pi} + L_{Bi}) \\ E_{Bi}I_{Bi}\phi''_{ij2}(L_{Pi} + L_{Bi}) &= -m_{Mi}d_{Mi}\omega_{ij}^2\phi'_{ij2}(L_{Pi} + L_{Bi}) - m_{Mi}\omega_{ij}^2\phi_{ij2}(L_{Pi} + L_{Bi}) \end{aligned} \right\} \text{ at } x = L_{Pi} + L_{Bi}, \quad (\text{A5})$$

where $d_i = a_i + b_i$ is the distance from the fixed point on the cantilever beam to the front face of the i th magnet, ω_{ij} is the natural frequency of the j th mode of the i th beam, $\omega_{ij}^2 = \beta_{ij2}^4 \frac{E_{Bi}I_{Bi}}{M_iL_{Bi}}$. Substitute Eq. (A1) and (A2) into Eqs. (A3)–(A5) to obtain the characteristic equation, and calculate the first three natural frequencies (shown in Table A1) corresponding to the first three zeros. Based on this characteristic equation, solve for the coefficients C_{ijk} , D_{ijk} , β_{ij1} , and β_{ij2} . Finally, C_{i1k} is solved through normalization conditions.

Table A1

The natural frequencies of the first three orders of Beam A and Beam B.

	ω_{i1} (rad/s)	ω_{i2} (rad/s)	ω_{i3} (rad/s)
Beam A	68.61	504.69	2716.22
Beam B	99.77	733.58	3499.28

The equivalent mass, equivalent damping, equivalent stiffness, electromechanical coupling coefficient, bending section coefficient, first moment of piezoelectric layer cross-section, and excitation coefficient are expressed as follows:

$$\begin{aligned} M_{eij} &= \rho_{Pi}A_{Pi} \int_0^{L_{Pi}} \phi_{ij1}^2(x)dx + \rho_{Bi}A_{Bi} \int_{L_{Pi}}^{L_{Bi}} \phi_{ij2}^2(x)dx \\ &+ m_{Mi}\phi_{ij2}^2(L_{Bi}) + 2m_{Mi}b_i^2\phi_{ij2}^2(L_{Bi}) + [I_{Mi} + m_{Mi}b_i^2]\phi_{ij2}^2(L_{Bi}), \end{aligned} \quad (\text{A6})$$

$$C_{eij} = c_i I_{Pi} \int_0^{L_{Pi}} \phi_{ij1}^2(x)dx + c_i I_{Bi} \int_{L_{Pi}}^{L_{Bi}} \phi_{ij2}^2(x)dx, \quad (\text{A7})$$

$$E_{eij} = E_{Ci}I_{Ci} \int_0^{L_{Pi}} \phi_{ij1}^2(x)dx + E_{Bi}I_{Bi} \int_{L_{Pi}}^{L_{Bi}} \phi_{ij2}^2(x)dx, \quad (\text{A8})$$

$$\theta_{Pij} = \frac{e_i H_{P_i} G_{P_j}}{h_{P_i}}, \quad (\text{A9})$$

$$G_{Pij} = \int_0^{L_{Pi}} \phi_{il}''(x)dx, \quad (\text{A10})$$

$$H_{Pi} = \iint_{S_{Pi}} z_i dS_{Pi}, \quad (\text{A11})$$

$$\Gamma_{ij} = \rho_i A_{i2} \int_0^{L_{Pi}} \phi_{ij1}(x)dx + \rho_i A_{i2} \int_{L_{Pi}}^{L_{Bi}} \phi_{ij2}(x)dx + M_i [\phi_{2i}(L_{Bi}) + (d_{1i} + d_{2i})\phi'_{ij2}(L_{Bi})]. \quad (\text{A12})$$

The magnetic potential energy is expressed as follows:

$$U_M(t) = -\frac{\mu_0 M_{M1} V_{M1} M_{M2} V_{M2}}{4\pi} \frac{-[w_1|_{x=L_B}(t) - w_2|_{x=L_B}(t)]^2 + 2(s + a_1 + a_2)^2}{[(s + a_1 + a_2)^2 + [w_1|_{x=L_{B1}}(t) - w_2|_{x=L_{B2}}(t)]^2]^{\frac{3}{2}}}, \quad (\text{A13})$$

The magnetic force between Magnet A and Magnet B is expressed as follows:

$$F_{M1}(t) = \frac{3\mu_0 M_{M1} V_{M1} M_{M2} V_{M2}}{4\pi} \frac{-4(s + a_1 + a_2)^2 [w_1|_{x=L_{B1}}(t) - w_2|_{x=L_{B2}}(t)] + [w_1|_{x=L_{B1}}(t) - w_2|_{x=L_{B2}}(t)]^3}{[(s + a_1 + a_2)^2 + [w_1|_{x=L_{B1}}(t) - w_2|_{x=L_{B2}}(t)]^2]^{\frac{3}{2}}}, \quad (\text{A14})$$

$$F_{M2}(t) = \frac{3\mu_0 M_{M1} V_{M1} M_{M2} V_{M2}}{4\pi} \frac{-4(s+a_1+a_2)^2 [w_1|_{x=L_{B1}}(t) - w_2|_{x=L_{B2}}(t)] + [w_1|_{x=L_{B1}}(t) - w_2|_{x=L_{B2}}(t)]^3}{[(s+a_1+a_2)^2 + [w_1|_{x=L_{B1}}(t) - w_2|_{x=L_{B2}}(t)]^2]^{\frac{7}{2}}} \quad (\text{A15})$$

The bending stiffness of the base beam and the composite beam are:

$$E_{Bi} I_{Bi} = E_{Bi} \frac{b_{Bi} h_{Bi}^3}{12}, \quad (\text{A16})$$

$$E_{Ci} I_{Ci} = E_{Bi} I_{Bi} + E_{Pi} I_{Pi} = b_{Bi} \left[E_{Bi} \frac{h_{Bi}^3}{12} + E_{Pi} \frac{\left(\frac{h_{Bi}}{2} + h_{Pi}\right)^3}{3} - \frac{h_{Bi}^3}{24} \right]. \quad (\text{A17})$$

The following transformations are defined: $[x_1(t), x_2(t), x_3(t)] = [\eta_{11}(t), \eta_{12}(t), \eta_{13}(t)]$ representing Beam A, $[x_4(t), x_5(t), x_6(t)] = [\eta_{21}(t), \eta_{22}(t), \eta_{23}(t)]$ representing Beam B, and $[x_{13}(t), x_{14}(t)] = [V_{P1}(t), V_{P2}(t)]$ representing the voltage output.

The electromechanical equations of the IMTPEH can be organized into the form of vector as follows:

$$\left\{ \begin{array}{l} \dot{x}_1(t) = x_2(t) \\ \dot{x}_2(t) = \left[F_{M1}(t) - \phi_{112}(L_{B1}) F_{S1}(L_{B1}, t) - \Gamma_{11} \ddot{w}_b(t) + \theta_{P11} x_{13}(t) - K_{e11} x_1(t) - C_{e11} x_2(t) \right] / M_{e11} \\ \dot{x}_3(t) = x_4(t) \\ \dot{x}_4(t) = \left[F_{M1}(t) - \phi_{122}(L_{B1}) F_{S1}(L_{B1}, t) - \Gamma_{12} \ddot{w}_b(t) + \theta_{P12} x_{13}(t) - K_{e12} x_3(t) - C_{e12} x_4(t) \right] / M_{e12} \\ \dot{x}_5(t) = x_6(t) \\ \dot{x}_6(t) = \left[F_{M1}(t) - \phi_{132}(L_{B1}) F_{S1}(L_{B1}, t) - \Gamma_{13} \ddot{w}_b(t) + \theta_{P13} x_{13}(t) - K_{e13} x_5(t) - C_{e13} x_6(t) \right] / M_{e13} \\ \dot{x}_7(t) = x_8(t) \\ \dot{x}_8(t) = \left[F_{M2}(t) - \phi_{212}(L_{B2}) F_{S2}(L_{B2}, t) - \Gamma_{21} \ddot{w}_b(t) + \theta_{P21} x_{14}(t) - K_{e21} x_7(t) - C_{e21} x_8(t) \right] / M_{e21} \\ \dot{x}_9(t) = x_{10}(t) \\ \dot{x}_{10}(t) = \left[F_{M2}(t) - \phi_{222}(L_{B2}) F_{S2}(L_{B2}, t) - \Gamma_{22} \ddot{w}_b(t) + \theta_{P22} x_{14}(t) - K_{e22} x_9(t) - C_{e22} x_{10}(t) \right] / M_{e22} \\ \dot{x}_{11}(t) = x_{12}(t) \\ \dot{x}_{12}(t) = \left[F_{M2}(t) - \phi_{232}(L_{B2}) F_{S2}(L_{B2}, t) - \Gamma_{23} \ddot{w}_b(t) + \theta_{P23} x_{14}(t) - K_{e23} x_{11}(t) - C_{e23} x_{12}(t) \right] / M_{e23} \\ \dot{x}_{13}(t) = [-x_{13}(t)/R_p - [\theta_{P11}, \theta_{P12}, \theta_{P13}] [x_2(t), x_4(t), x_6(t)]^T] / C_p \\ \dot{x}_{14}(t) = [-x_{14}(t)/R_p - [\theta_{P21}, \theta_{P22}, \theta_{P23}] [x_8(t), x_{10}(t), x_{12}(t)]^T] / C_p \end{array} \right. \quad (\text{A18})$$

Appendix B

The variation of equilibrium position of the magnets with the increase of the magnet distance is calculated by solving the static homogenous equations as follows:

$$F_{M1} + K_{11} w_1|_{x=L_{B1}} = 0, \quad (\text{A19})$$

$$F_{M2} + K_{21} w_2|_{x=L_{B2}} = 0, \quad (\text{A20})$$

where K_{11} and K_{21} are the equivalent stiffness of the first mode of Beam A and Beam B, respectively.

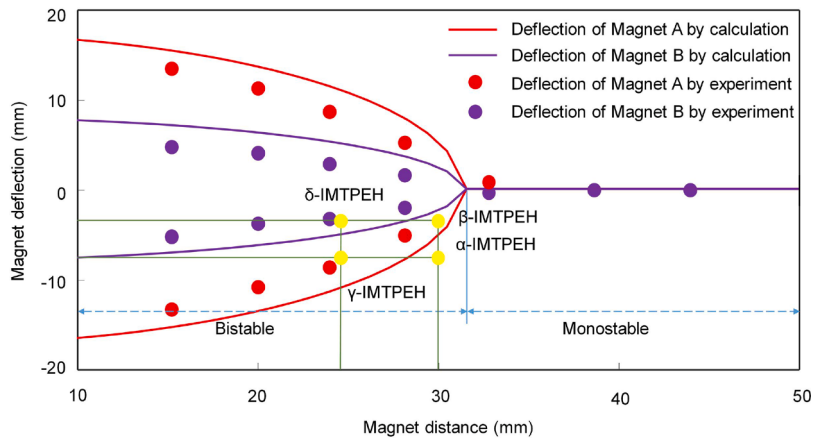


Fig. A1. Bifurcation diagram of the static equilibrium state of two beams with respect to the magnet distance. The solid red and purple lines represent the calculated values of Magnet A and Magnet B, respectively, and the red and purple dots represent the measured values of Magnet A and Magnet B. The threshold value of between the monostable and bistable is 32 mm.

The measurement method for the deviation of two magnets is referred to the paper [38]. Fig. A1 shows the bifurcation diagram of the static equilibrium state of magnets with respect to the magnet distance by solving (A16) and (A17) simultaneously. When the distance between the magnets decreases to a critical value, the two beams transition from a monostable state to a bistable state. And as the distance between the magnets decreases, the offset of the magnets increases. The offset of Magnet A is greater than that of Magnet B, because the stiffness of Beam A is smaller than that of Beam B. Under the same repulsive force, the deformation of Beam A is greater than that of Beam B. The measured values and calculated values can match well, which confirms the feasibility of the magnetic force calculation formula. The yellow dots in Fig. A1 represent the positions of the four configurations in the bifurcation diagram. For α-IMTPEH, the stop block does not change the static position of the two beams, while for δ-IMTPEH, the stop block restricts the two beams from resting in the static equilibrium position.

Appendix C

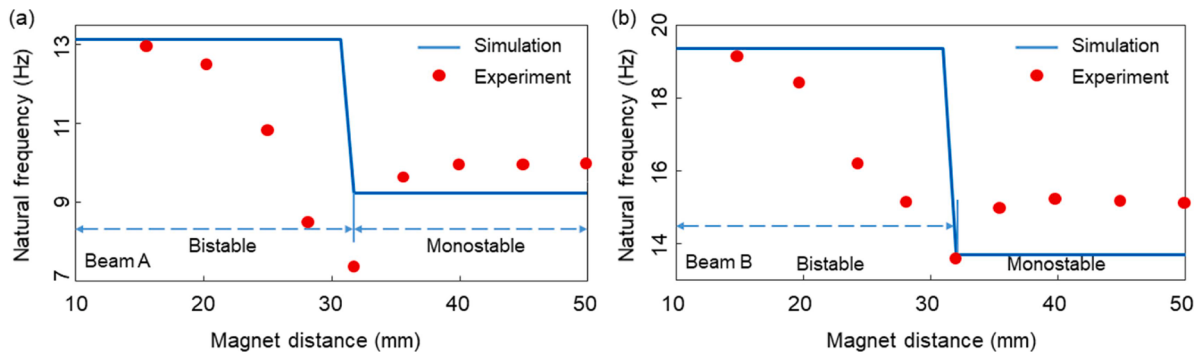


Fig. A2. The simulated and experimental results of the natural frequency varying with the magnet distance. Results of (a) Beam A and (b) Beam B. The solid blue line represents the simulated value, and the red dots represent the measured value.

The magnetic force of the interaction between magnets can be regarded as a magnetic spring applied to a cantilever beam, therefore, the magnetic force can be rewritten as:

$$F_{M1}(t) = \kappa_1(t)w_1|_{x=L_{B1}}(t), \quad (\text{A21})$$

$$F_{M2}(t) = \kappa_2(t)w_2|_{x=L_{B2}}(t), \quad (\text{A22})$$

where κ_1 and κ_2 are the magnetic spring coefficients as follows:

$$\kappa_1(t) = \frac{3\mu_0 M_{M1} V_{M1} M_{M2} V_{M2}}{4\pi} \frac{-4(s+a_1+a_2)^2 [w_1|_{x=L_{B1}}(t) - w_2|_{x=L_{B2}}(t)] + [w_1|_{x=L_{B1}}(t) - w_2|_{x=L_{B2}}(t)]^3}{[(s+a_1+a_2)^2 + [w_1|_{x=L_{B1}}(t) - w_2|_{x=L_{B2}}(t)]^2]^{\frac{7}{2}}} / w_1|_{x=L_{B1}}(t), \quad (\text{A23})$$

$$\kappa_2(t) = \frac{3\mu_0 M_{M1} V_{M1} M_{M2} V_{M2}}{4\pi} \frac{-4(s+a_1+a_2)^2 [w_1|_{x=L_{B1}}(t) - w_2|_{x=L_{B2}}(t)] + [w_1|_{x=L_{B1}}(t) - w_2|_{x=L_{B2}}(t)]^3}{[(s+a_1+a_2)^2 + [w_1|_{x=L_{B1}}(t) - w_2|_{x=L_{B2}}(t)]^2]^{\frac{7}{2}}} / w_2|_{x=L_{B2}}(t). \quad (\text{A24})$$

The nonlinear natural frequencies f_{n1}, f_{n2} of two beams under the effect of the magnet field can be calculated [38]:

$$f_{n1}(t) = \frac{1}{2\pi} \sqrt{\frac{K_{11} + \kappa_1(t)}{M_{e1}}}, \quad (\text{A25})$$

$$f_{n2} = \frac{1}{2\pi} \sqrt{\frac{K_{21} + \kappa_2(t)}{M_{e2}}}. \quad (\text{A26})$$

By calculating Eqs. (A21) and (A22), the natural frequencies of two beams are obtained as shown in Fig. A2. Two beams were given an initial deformation to generate free motion, and the vibration frequency of the cantilever beam were obtained by measuring the voltage generated by the piezoelectric patches attached to the surface of the cantilever beams. When the magnet distance is far enough, such as in the simulation results, greater than 32 mm, the natural frequencies of the two beams are linear natural frequencies. When the distance between the magnets is less than the critical value, which is 32 mm, the natural frequencies of the two beams are significantly increased due to the effect of the magnets. A similar trend can be observed from the experimental results. However, in the experimental results, as the distance between the magnets decreases, the natural frequency of Beam A first decreases and then increases, with a minimum frequency around 31 mm. This characteristic conforms to the pattern in the paper [38]. Although there is a certain deviation between the theoretical and experimental results, the theoretical results can still reflect the main characteristics of the natural frequency changes of the system under the action of magnets.

Appendix D

To demonstrate that taking the first three modes of simulation is better than taking the first two modes in this problem, the first mode, second mode, third mode, and experimental results are compared in Fig. A3. The experimental results selected are the results in Fig. 10(d). From Fig. A3 shows that taking the third-order mode is more specific in reflecting the waveform details of the high-frequency response generated by collisions, while only taking the first two modes results in a lot of information loss on the collision waveform. The fourth order mode and modes above tend to take the waveform response of the third order mode, but it greatly increases the computational complexity. Therefore, we selected the first three modes of the cantilever beam for system simulation while considering reflecting the collision waveform and computational complexity as much as possible.

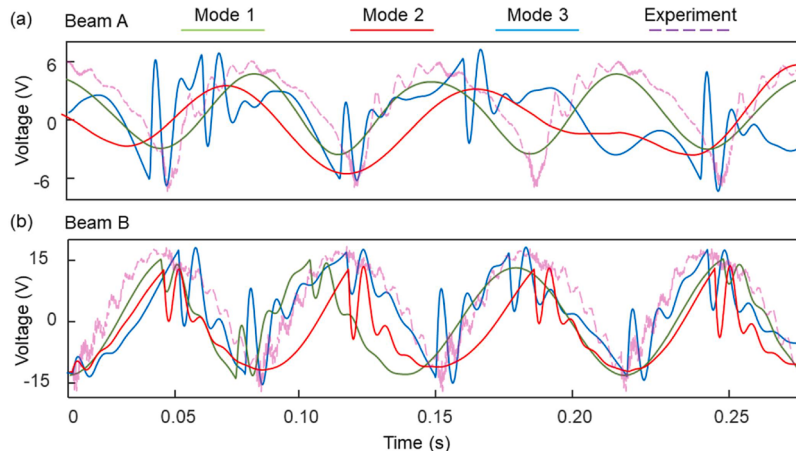


Fig. A3. Comparison of simulation and experimental results. Green, red, and blue solid lines represent the calculated voltage responses of cantilever beams with first-, second-, and third-order modes, respectively; the purple dashed line represents the experimental value.

References

- [1] Cao H, Tang M, Zhang Z, Tairab AM, Mutsuda H, Wu X. A magnetic coupling wind energy harvester for unmanned surface vehicles. *Int J Mech Sci* 2023;257:108543.
- [2] Yang Z, Zhou S, Zu J, Inman D. High-performance piezoelectric energy harvesters and their applications. *Joule* 2018;2:642–97.
- [3] Luo A, Xu W, Sun J, Xi K, Tang S, Guo X, Lee C, Wang F. Vibration energy harvester with double frequency-up conversion mechanism for self-powered sensing system in smart city. *Nano Energy* 2023;105:108030.
- [4] Liao W, Wen Y, Kan J, Huang X, Wang S, Li Z, Zhang Z. A joint-nested structure piezoelectric energy harvester for high-performance wind-induced vibration energy harvesting. *Int J Mech Sci* 2022;227:107443.
- [5] Han Y, Wu F, Du X, Li Z, Chen H, Guo D, Wang J, Yu H. Enhance vortices vibration with Y-type bluff body to decrease arousing wind speed and extend range for flag triboelectric energy harvester. *Nano Energy* 2024;119:109063.
- [6] Li Z, Peng Y, Xu Z, Peng J, Xin L, Wang M, Luo J, Xie S, Pu H. Harnessing energy from suspension systems of oceanic vehicles with high-performance piezoelectric generators. *Energy* 2021;228:120523.
- [7] Li Z, Zu J, Yang Z. Introducing hinge mechanisms to one compressive-mode piezoelectric energy harvester. *J Renew Sustain Energy* 2018;10.
- [8] Pan Q, Wang B, Zhang L, Li Z, Yang Z. Whisk-inspired motion converter for ocean wave energy harvesting. *IEEE ASME Trans Mechatron* 2022;27:1808–11.
- [9] Su X, Xu J, Chen X, Sun S, Lee DG, Zhu B, Baik JM, Hur S, Fan S, Song HC, Leng Y. A piezoelectric-electromagnetic hybrid energy harvester with frequency-up conversion mechanism towards low-frequency-low-intensity applications. *Nano Energy* 2024;124:109447.
- [10] Shen F, Li Z, Xin C, Guo H, Peng Y, Li K. Interface defect detection and identification of triboelectric nanogenerators via voltage waveforms and artificial neural network. *ACS Appl Mater Interfaces* 2022;14:3437–45.
- [11] Bai Q, Zhou T, Gan C, Wang Q, Zheng X, Wei KX. A triboelectric-piezoelectric hybrid nanogenerator for rotational energy harvesting based on bistable cantilever beam. *Energy Convers Manag* 2024;300:117971.
- [12] Sani G, Balaram B, Kudra G, Awrejcewicz J. Energy harvesting from friction-induced vibrations in vehicle braking systems in the presence of rotary unbalances. *Energy* 2024;289:130007.
- [13] Peng Y, Zhang D, Luo J, Xie S, Pu H, Li Z. Power density improvement based on investigation of initial relative position in an electromagnetic energy harvester with self-powered applications. *Smart Mater Struct* 2021;30:065005.
- [14] Du X, Chen H, Li C, Li Z, Wang W, Guo D, Yu H, Wang J, Tang L. Wake galloping piezoelectric-electromagnetic hybrid ocean wave energy harvesting with oscillating water column. *Appl Energy* 2024;353:122081.
- [15] He L, Liu R, Liu X, Zheng X, Zhang L, Lin J. A piezoelectric-electromagnetic hybrid energy harvester for low-frequency wave motion and self-sensing wave environment monitoring. *Energy Convers Manag* 2024;300:117920.
- [16] Rajarathinam M, Awrejcewicz J, Ali SF. A novel design of an array of pendulum-based electromagnetic broadband vibration energy harvester. *Mech Syst Sig Process* 2024;208:110955.
- [17] Sezer N, Koç M. A comprehensive review on the state-of-the-art of piezoelectric energy harvesting. *Nano Energy* 2021;80:105567.

- [18] He L, Liu R, Liu X, Zhang Z, Zhang L, Cheng G. A novel piezoelectric wave energy harvester based on cylindrical-conical buoy structure and magnetic coupling. *Renew Energy* 2023;210:397–407.
- [19] Wan C, Tian H, Shan X, Xie TJLJOMS. Enhanced performance of airfoil-based piezoelectric energy harvester under coupled flutter and vortex-induced vibration. *Int J Mech Sci* 2023;241:107979.
- [20] Cao Y, Zheng Y, Mei X, Dong F, Xu R, Shi C, Zhang P, Wei K, Li Y. Modelling and analysis of a novel E-shape piezoelectric vibration energy harvester with dynamic magnifier. *Mech Res Commun* 2024;137:104257.
- [21] Chen K, Zhang X, Xiang X, Shen H, Yang Q, Wang J, Litak G. High performance piezoelectric energy harvester with dual-coupling beams and bistable configurations. *J Sound Vib* 2023;561:117822.
- [22] Liu Z, Chen Y, Wang X, Yu X, Dai H, Shi Z, Wan H, Wei X, Huan R. Nonlinearity enhanced mode localization in two coupled MEMS resonators. *Int J Mech Sci* 2024; 271:109133.
- [23] Mangalasseri AS, Mahesh V, Mukunda S, Ponnuasami S, Harursampath D, Tounsi AJAINR. Vibration based energy harvesting performance of magneto-electro-elastic beams reinforced with carbon nanotubes. *Adv Nano Res* 2023;14:27–43.
- [24] Shim HK, Sun S, Kim HS, Lee DG, Lee YJ, Jang JS, Cho KH, Baik JM, Kang CY, Leng Y, Hur S, Song HC. On a nonlinear broadband piezoelectric energy harvester with a coupled beam array. *Appl Energy* 2022;328:120129.
- [25] Xie X, Zhang J, Wang Z, Li L, Du G. The effect of magnetic proof masses on the energy harvesting bandwidth of piezoelectric coupled cantilever array. *Appl Energy* 2024;353:122042.
- [26] Panyam M, Daqaq MF. Characterizing the effective bandwidth of tri-stable energy harvesters. *J Sound Vib* 2017;386:336–58.
- [27] Sun X, Qian J, Xu J. Compressive-sensing model reconstruction of nonlinear systems with multiple attractors. *Int J Mech Sci* 2024;265:108905.
- [28] Zhou K, Dai HL, Abdelkefi A, Ni Q. Theoretical modeling and nonlinear analysis of piezoelectric energy harvesters with different stoppers. *Int J Mech Sci* 2020;166: 105233.
- [29] Wang S, He L, Wang H, Li X, Sun B, Lin J. Energy harvesting from water impact using piezoelectric energy harvester. *Rev Sci Instrum* 2024;95.
- [30] Devarajan K, Santhosh B. Performance enhancement of snap-through vibration energy harvester with displacement amplifier. *Int J Mech Sci* 2023;253:108391.
- [31] Liu H, Zhao X, Liu H, Yang J. Magnetostrictive biomechanical energy harvester with a hybrid force amplifier. *Int J Mech Sci* 2022;233:107652.
- [32] Wang M, Liu J, Peng Y, Li Z. Investigation of nonlinear magnetic stiffness based thin-layer stacked piezoelectric generators with a force-amplification structure. *Thin Walled Struct* 2024;195:111525.
- [33] Zayed AA, Assal SF, Nakano K, Kaizuka T, Fath El-Bab AM. Design procedure and experimental verification of a broadband quad-sTable 2-DOF vibration energy harvester. *Sensors* 2019;19:2893.
- [34] Wang JX, Li JC, Su WB, Zhao X, Wang CM. A multi-folded-beam piezoelectric energy harvester for wideband energy harvesting under ultra-low harmonic acceleration. *Energy Rep* 2022;8:6521–9.
- [35] Velusamy VR, Foong FM, Nik Mohd NAR, Thein CK. Bistable dual cantilever flutter for potential wind energy harvesting applications. *Sustain Energy Technol Assess* 2024;63:103637.
- [36] Cao J, Wang W, Zhou S, Inman DJ, Lin J. Nonlinear time-varying potential bistable energy harvesting from human motion. *Appl Phys Lett* 2015;107:143904.
- [37] Xing J, Fang S, Fu X, Liao WH. A rotational hybrid energy harvester utilizing bistability for low-frequency applications: modelling and experimental validation. *Int J Mech Sci* 2022;222:107235.
- [38] Atmeh M, Ibrahim A, Ramini A. Static and dynamic analysis of a bistable frequency up-converter piezoelectric energy harvester. *Micromachines* 2023;14:261 (Basel).
- [39] Ibrahim A, Towfighian S, Younis MI. Dynamics of transition regime in bistable vibration energy harvesters. *J Vib Acoust* 2017;139:051008.
- [40] Liu H, Zhao L, Chang Y, Shan G, Gao Y. Parameter optimization of magnetostrictive bistable vibration harvester with displacement amplifier. *Int J Mech Sci* 2022;223: 107291.
- [41] Jiang Q, Yu C, Zhou Y, Zhao Z, Gao Q, Sun B. Modeling and analysis of beam-spring magnetically coupled bistable energy harvester for broadband vibration energy harvesting. *J Sound Vib* 2024;579:118373.
- [42] Li Q, Bu L, Lu S, Yao B, Huang Q, Wang X. Practical asymmetry and its effects on power and bandwidth performance in bi-stable vibration energy harvesters. *Mech Syst Sig Process* 2024;206:110939.
- [43] Zhang J, Zhi Y, Yang K, Hu N, Peng Y, Wang B. Internal resonance characteristics of a bistable electromagnetic energy harvester for performance enhancement. *Mech Syst Sig Process* 2024;209:111136.
- [44] Norenberg JP, Luo R, Lopes VG, Peterson JVLL, Cunha A. Nonlinear dynamic of asymmetric bistable energy harvesters. *Int J Mech Sci* 2023;257:108542.
- [45] Liu C, Zhang W, Yu K, Liao B, Zhao R, Liu T. Gravity-induced biTable 2DOF piezoelectric vibration energy harvester for broadband low-frequency operation. *Arch Civ Mech Eng* 2023;23:208.
- [46] Sun S, Leng Y, Su X, Zhang Y, Xu J. Performance of a novel dual-magnet tri-stable piezoelectric energy harvester subjected to random excitation. *Energy Convers Manag* 2021;239:114246.
- [47] Wang G, Zhao Z, Liao WH, Tan J, Ju Y, Li Y. Characteristics of a tri-stable piezoelectric vibration energy harvester by considering geometric nonlinearity and gravitation effects. *Mech Syst Sig Process* 2020;138:106571.
- [48] Li HT, Ding H, Jing XJ, Qin WY, Chen LQ. Improving the performance of a tri-stable energy harvester with a staircase-shaped potential well. *Mech Syst Sig Process* 2021;159:107805.
- [49] Chen W, Zhang Q, Wei W, Feng J. A low-frequency, wideband quad-stable energy harvester using combined nonlinearity and frequency up-conversion by cantilever-surface contact. *Mech Syst Sig Process* 2018;112:305–18.
- [50] Mei X, Zhou S, Yang Z. Enhancing energy harvesting in low-frequency rotational motion by a quad-stable energy harvester with time-varying potential wells. *Mech Syst Sig Process* 2021;148:107167.
- [51] Zhou Z, Qin W, Yang Y, Zhu P. Improving efficiency of energy harvesting by a novel penta-stable configuration. *Sens Actuators A* 2017;265:297–305.
- [52] Zhang Y, Duan J, Jin Y, Li Y. Discovering governing equation from data for multi-stable energy harvester under white noise. *Nonlinear Dyn* 2021;106:2829–40.
- [53] Costa LG, Savi MA. Nonlinear Dyn. of a compact and multistable mechanical energy harvester. *Int J Mech Sci* 2024;262.
- [54] Fan Y, Ghayesh MH, Lu TF, Amabili M. Design, development, and theoretical and experimental tests of a nonlinear energy harvester via piezoelectric arrays and motion limiters. *Int J Non Linear Mech* 2022;142:103974.
- [55] Ibrahim A, Ramini A, Towfighian S. Experimental and theoretical investigation of an impact vibration harvester with triboelectric transduction. *J Sound Vib* 2018; 416:111–24.
- [56] Jiang W, Wang L, Zhao L, Luo G, Yang P, Ning S, Lu D, Lin Q. Modeling and design of V-shaped piezoelectric vibration energy harvester with stopper for low-frequency broadband and shock excitation. *Sens Actuators A* 2021;317:112458.
- [57] Wang S, Yang Z, Kan J, Chen S, Chai C, Zhang Z. Design and characterization of an amplitude-limiting rotational piezoelectric energy harvester excited by a radially dragged magnetic force. *Renew Energy* 2021;177:1382–93.
- [58] Zhou K, Dai H, Abdelkefi A, Ni Q. Theoretical modeling and nonlinear analysis of piezoelectric energy harvesters with different stoppers. *Int J Mech Sci* 2020;166: 105233.
- [59] Machado SP, Febbo M, Ramirez JM, Gatti CD. Rotational double-beam piezoelectric energy harvester impacting against a stop. *J Sound Vib* 2020;469: 115141.
- [60] Xiao Y, Wu N, Wang Q. Analysis of a friction-induced vibration piezoelectric energy generator under linear, bi-linear, and impact conditions. *Int J Mech Sci* 2024;109148.
- [61] Tan D, Zhou J, Wang K, Ouyang H, Zhao H, Xu D. Sliding-impact bistable triboelectric nanogenerator for enhancing energy harvesting from low-frequency intrawell oscillation. *Mech Syst Sig Process* 2023;184:109731.
- [62] Fang S, Chen K, Lai Z, Zhou S, Liao WH. Analysis and experiment of auxetic centrifugal softening impact energy harvesting from ultra-low-frequency rotational excitations. *Appl Energy* 2023;331:120355.
- [63] Bahmanziari S, Zamani AA. A new framework of piezoelectric smart tiles based on magnetic plucking, mechanical impact, and mechanical vibration force mechanisms for electrical energy harvesting. *Energy Convers Manag* 2024;299: 117902.
- [64] Xu J, Xia D, Lai Z, Chen G, Dai W, Wang J, Yang H. Experimental study of vibration modes switching based triple frequency-up-converting energy harvesting with pre-biased displacement. *Smart Mater Struct* 2024.
- [65] Sokolov A, Galayko D, Basset P, Blokhina E. On the frequency up-conversion mechanism due to a soft stopper by the example of an electrostatic kinetic energy harvester. *J Intell Mater Syst Struct* 2022;34:696–705.
- [66] Alvis T, Abdelkefi A. Efficacy of vibro-impact energy harvesting absorbers on controlling dynamical systems under vortex-induced vibrations and base excitation. *Ocean Eng* 2023;272:113816.
- [67] He Q, Xu Z, Sun S, Zhou M, Wang Y, Ji H. A novel two-degree-of-freedom nonlinear piezoelectric energy harvester with a stopper for broadband low-frequency vibration. *AIP Adv* 2023;13.
- [68] Hassan M, Ibrahim A. A two-degree-of-freedom vibro-impact triboelectric energy harvester for larger bandwidth. *J Sound Vib* 2023;563:117798.
- [69] Shao N, Xu J, Xu X. Experimental study of a two-degree-of-freedom piezoelectric cantilever with a stopper for broadband vibration energy harvesting. *Sens Actuators A* 2022;344:113742.
- [70] Zhang B, Li H, Zhou S, Liang J, Gao J, Yurchenko D. Modeling and analysis of a three-degree-of-freedom piezoelectric vibration energy harvester for broadening bandwidth. *Mech Syst Sig Process* 2022;176:109169.
- [71] Li X, Zhang J, Li R, Dai L, Wang W, Yang K. Dynamic responses of a two-degree-of-freedom bistable electromagnetic energy harvester under filtered band-limited stochastic excitation. *J Sound Vib* 2021;511:116334.
- [72] Wang H, Tang L. Modeling and experiment of bistable two-degree-of-freedom energy harvester with magnetic coupling. *Mech Syst Sig Process* 2017;86:29–39.
- [73] Kim J, Lee DM, Ryu H, Kim YJ, Kim H, Yoon HJ, Kang M, Kwak SS, Kim SW. Triboelectric nanogenerators for battery-free wireless sensor system using multi-degree of freedom vibration. *Adv Mater Technol* 2024;9:2301427.
- [74] Zhang J, Zhang J, Zhang B, An Y, Yang X, Hu N, Ma L, Peng Y, Wang B. Broadband multifrequency vibration attenuation of an acoustic metamaterial beam with two-degree-of-freedom nonlinear bistable absorbers. *Mech Syst Sig Process* 2024;212: 111264.
- [75] Hao D, Gong Y, Wu J, Shen Q, Zhang Z, Zhi J, Zou R, Kong W, Kong L. A self-sensing and self-powered wearable system based on multi-source human motion energy harvesting. *Small* 2024;231103.
- [76] Ma X, Zhang H, Margielewicz J, Gąska D, Wolszczak P, Litak G, Zhou S. A dual-beam piezo-magneto-elastic wake-induced vibration energy harvesting system for high-performance wind energy harvesting. *Sci China Technol Sci* 2023;67:221–39.
- [77] He L, Kurita H, Narita F. Multimode auxetic piezoelectric energy harvester for low-frequency vibration. *Smart Mater Struct* 2024;33.
- [78] Ding J, Zhou D, Wang M, Li Z, Sun Y, Pu H, Pan Q, Wang B. Fractal-inspired multifrequency piezoelectric energy harvesters. *Appl Phys Lett* 2024;124.

- [79] Fan Y, Zhang Y, Niu MQ, Chen LQ. An internal resonance piezoelectric energy harvester based on geometrical nonlinearities. *Mech Syst Sig Process* 2024;211:111176.
- [80] Liu J, Bao B, Chen J, Wu Y, Wang Q. Marine energy harvesting from tidal currents and offshore winds: a 2-DOF system based on flow-induced vibrations. *Nano Energy* 2023;114:108664.
- [81] He L, Gu X, Hou Y, Hu R, Zhou J, Cheng G. A piezoelectric energy harvester for collecting environment vibration excitation. *Renew Energy* 2022;200:537–45.
- [82] Zhang J, Wu M, Wu H, Ding S. An asymmetric bistable vibro-impact DEG for enhanced ultra-low-frequency vibration energy harvesting. *Int J Mech Sci* 2023;255:108481.
- [83] Tian L, Shen H, Yang Q, Song R, Bian Y. A novel outer-inner magnetic two degree-of-freedom piezoelectric energy harvester. *Energy Convers Manag* 2023;283:116920.
- [84] Cong M, Gao Y, Wang W, He L, Mao X, Long Y, Dong W. Asymmetry stagger array structure ultra-wideband vibration harvester integrating magnetically coupled nonlinear effects. *Appl Energy* 2024;356:116920.
- [85] Shao N, Chen Z, Wang X, Zhang C, Xu J, Xu X, Yan R. Modeling and analysis of magnetically coupled piezoelectric dual beam with an annular potential energy function for broadband vibration energy harvesting. *Nonlinear Dyn* 2023;111:11911–37.
- [86] Noh J, Nguyen MS, Kim P, Yoon YJ. Harmonic balance analysis of magnetically coupled two-degree-of-freedom bistable energy harvesters. *Sci Rep* 2022;12:6221.
- [87] Li G, Wang G, Zhou Y, Hou L, Jiang Y. A novel M-shaped 2-DOF piezoelectric energy harvester with built-in outer-inner magnetic tri-stable oscillators for energy converting enhancement and applications. *Mech Syst Sig Process* 2024;208:111055.
- [88] Stanton SC, McGehee CC, Mann BP. Nonlinear Dyn. for broadband energy harvesting: investigation of a bistable piezoelectric inertial generator. *Phys D* 2010;239:640–53.